Summer 7-1-2022

Measurement of |vcb| Using the Semileptonic Decay Λb → Λcμνμ

Scott Edward Ely
Syracuse University

Recommended Citation

Ely, Scott Edward, "Measurement of |vcb| Using the Semileptonic Decay Λb → Λcμνμ" (2022).
Dissertations - ALL. 1552.
https://surface.syr.edu/etd/1552

Abstract

A preliminary measurement of the quark-mixing parameter $|V_{cb}|$ using the exclusive decay $\Lambda_b^0 \to \Lambda_c^+ \mu^- \overline{\nu}_\mu$ is presented. A sample of Λ_b semileptonic decays is provided by $\sqrt{s} = 13TeV$ proton-proton collisions collected by the LHCb detector in 2017. $\Lambda_b^0 \to \Lambda_c^+ \mu^- \overline{\nu}_\mu X$ decays are identified from muon tracks, combined with a Λ_c baryon. The ground state $\Lambda_b^0 \to \Lambda_c^+ \mu^- \overline{\nu}_\mu$ is isolated by a fit to the Λ_b corrected mass spectrum. The raw yield $N_{Raw}(\Lambda_b^0 \to \Lambda_c^+ \mu^- \overline{\nu}_\mu)$ is corrected, and the semileptonic width $\Gamma_{Meas.}(\Lambda_b^0 \to \Lambda_c^+ \mu^- \overline{\nu}_\mu)$ is obtained. Lattice QCD calculations predict $\Gamma_{Th.}(\Lambda_b^0 \to \Lambda_c^+ \mu^- \overline{\nu}_\mu)/|V_{cb}|^2$. A comparison between the measured and predicted widths gives $|V_{cb}|$ from the relative normalization. This method also provides a measurement of the branching fraction $\mathcal{B}(\Lambda_b^0 \to \Lambda_c^+ \mu^- \overline{\nu}_\mu)$ using well-measured properties of B-meson decays.

Measurement of $|V_{cb}|$ using the Semileptonic Decay $\Lambda_b \to \Lambda_c \mu \overline{\nu}_\mu$

by

Scott Ely

B.S., University of California: Santa Cruz, 2012

Dissertation

Submitted in partial fulfillment of the requirements for the degree of Doctor of Philosophy in Physics

Syracuse University

July 2022

Acknowledgements

First and foremost, I extend my gratitude to my advisor, Marina Artuso, for her mentoring and guidance through out my Ph.D. program. Without her countless hours spent working both in physics analysis tasks, as well as detector hardware development, I would not have grown into the physicist I am today.

I also extend my thanks to the professors, post-doctoral researchers, and fellow graduate students, past and present, of the Syracuse University LHCb group, for their engaging discussions and for providing a friendly, welcoming working atmosphere. I would also like to thank my colleagues based at CERN for their efforts in guiding and supporting both my analysis efforts and their work towards the UT Upgrade project. I would especially like to thank Aravindhan Venkateswaran for his patience and good humor as we adjusted to a drastically new environment at CERN in March of 2020.

I thank the staff in the Syracuse University Physics department for ensuring that I had the resources necessary to be a proficient researcher, and for helping to make for a smooth transition between being based at Syracuse to Geneva.

I greatly appreciate the time and effort given by the examination committee for the review of this thesis.

And last, but certainly not least, I would like to thank my family for their love and encouragement, and for providing a strong sense of home despite being so far away. I would like to thank my father, Gary Ely, for reminding me to be steadfast and face my challenges with courage, and my mother, Therese Ely, for reminding me to look for the natural beauty in all that's around me. Finally, I would like to thank my devoted partner, Alexandra Steadman, who's love and support inspires me to be the best version of myself every day.

Contents

List of Figures

List of Tables

1 Introduction

1.1 The Standard Model

The Standard Model (SM) of particle physics (Figure 1) is the theoretical framework that describes all known fundamental particles and their interactions. It is the gauge group that couples the unified electroweak interaction, described by the symmetry group $SU(2) \otimes U(1)$, with the $SU(3)$ group used by QCD to describe the octet of color-gluons as the strong-force carriers. While robust, the theory does have shortcomings: there is no accounting for gravity as a fundamental force, nor does it include any descriptor of dark-matter. Furthermore, the amount of CP violation as predicted by the SM fails to justify the imbalance of matter to antimatter in the universe. To help resolve this discrepancy, investigations of CP-violating decays are important to make precision measurements of the parameters that support the SM description of nature, and in searches for phenomena that go beyond the Standard Model.

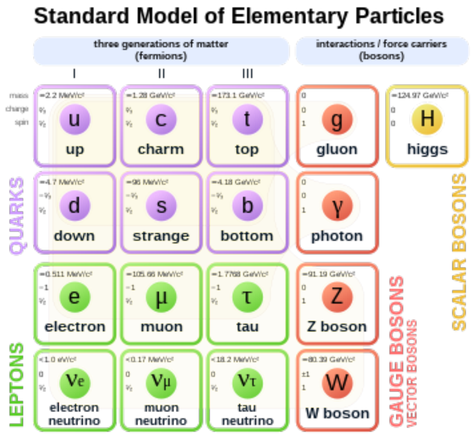

Figure 1: The Standard Model of Particle physics showing the three generations of matter, as well as gauge bosons.

1.2 The Cabbibo-Kobayashi-Maskawa Matrix

The electroweak coupling strength of the W boson to quarks in the Standard Model is described by the Cabbibo-Kobayashi-Maskawa (CKM) matrix V below:

$$\begin{pmatrix} d' \\ s' \\ b' \end{pmatrix} = \begin{pmatrix} V_{ud} & V_{us} & V_{ub} \\ V_{cd} & V_{cs} & V_{cb} \\ V_{td} & V_{ts} & V_{tb} \end{pmatrix} \begin{pmatrix} d \\ s \\ b \end{pmatrix} \tag{1}$$

It includes information on the strength of Flavor-Changing Neutral Currents (FCNC) in weak decays, which are suppressed in the SM. The CKM matrix is a 3x3 complex unitary matrix parameterized by three rotation angles and one phase factor of the form $e^{i\delta}$. The presence of this complex phase factor is the originator for CP violation in the SM [4]. Most elements of the CKM matrix are real, or close to real, with the exception of V_{tb} and V_{ub}. Thus, the unitarity condition

$$\sum_i = V_{i,j} V^*_{k,i} = \sum_i V^*_{j,i} V_{i,k} = \delta_{jk} \tag{2}$$

where one vanishing component is commonly written as

$$V_{ud} V^*_{ub} + V_{cd} V^*_{cb} + V_{td} V^*_{tb} = 0 \tag{3}$$

If each term in the above expression is treated as a vector, then the sum of these three vectors should be zero according to equation 3, and form a triangle when plotted in the complex plane. This is the famous Unitarity Triangle (UT). The UT is scaled and rotated such that $V_{cd} V^*_{cb}$ is real with unit magnitude (Fig. 2). Information of the CP-violating effects are contained with the three angles of the triangle:

$$\alpha = arg\big[-\frac{V_{td} V^*_{tb}}{V_{ud} V^*_{ub}}\big],\ \beta = arg\big[-\frac{V_{cd} V^*_{cb}}{V_{td} V^*_{tb}}\big],\ \gamma = arg\big[-\frac{V_{ud} V^*_{ub}}{V_{cd} V^*_{cb}}\big], \tag{4}$$

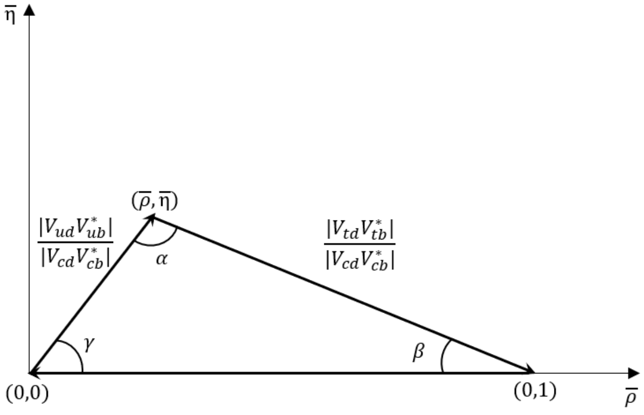

Figure 2: The Unitarity Triangle.

Tests of the unitarity nature of the CKM matrix can be performed based on independent determinations of its elements, leading to precise measurements of the three unitarity angles and to check overall agreement with the SM. Groups such as the Heavy Flavor Averaging Group (HFLAV), UT Fit, and CKMFitter provide the most up-to-date measurements of CKM parameters, as seen in figure 3.

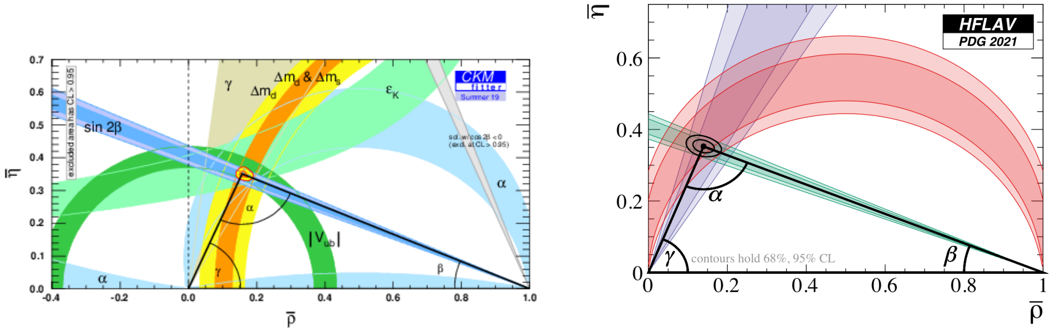

Figure 3: Current fits of the Unitarity triangle from CKMFitter [1] (left) and HFLAV [2](right).

1.2.1 The Quark-Mixing Parameter V_{cb}

Precision measurements of the quark mixing parameters that form the CKM matrix are vital for probing CP-violating effects in the SM. From Figure 2 it is clear that the side opposite to the angle β is proportional to the ratio $|V_{ub}|/|V_{cb}|$. Semileptonic B decays provide a promising avenue to measure these CKM elements, as they are predominantly a result of W-boson exchange. A precise determination of $|V_{cb}|$ is particularly interesting for rare decays, such as $B_s^0 \to \mu^+\mu^-$ which depends on $|V_{cb}|^2$, or in determining the CP-violationg parameter ε_K in Kaon decays, like $K^+ \to \pi^+\nu\overline{\nu}$ which depend on $|V_{cb}|^3$ or $K_L \to \pi^0\nu\overline{\nu}$ and $K_s \to \mu^+\mu^-$ which scale with $|V_{cb}|^4$ [6].

Two experimental approaches have been used to measure $|V_{cb}|$. The first so-called *inclusive method* (Fig. 4) exploits properties of the final state from $b \to X_c l\nu$ decays, such as the lepton energy or invariant mass of the hadron recoiling off of the lepton-neutrino pair, to extract $|V_{cb}|$ without reconstructing the final state hadron. The second approach is the *exclusive method*, in which a specific hadron is reconstructed in the final state. A long-standing tension between the two approaches exists, as $|V_{cb}|$ is observed with a 3σ discrepancy depending on the method used, leading to large uncertainties in measured quantities that depend on $|V_{cb}|$, like the ones previously described. Figure 5 illustrates this tension, and the current values are summarized in table 1.

1.2.2 Heavy Quark Effective Theory and Lattice QCD Predictions

Numerous measurements of CKM parameters have been performed, which over-constrain the consistency with the SM. However, subtle effects that go beyond the SM may exist, and tensions between existing measurements remain. Therefore, more precise measurements of $|V_{cb}|$ are required. Semileptonic decay

Table 1: Fit results from CKMFitter [1] Summer 2021 showing the tension between inclusive and exclusive determinations of $|V_{cb}|$.

Measurement	Result
$\|V_{cb}\|(exclusive)$	$(39.09 \pm 0.68) \times 10^{-3}$
$\|V_{cb}\|(inclusive)$	$(42.16 \pm 0.50) \times 10^{-3}$

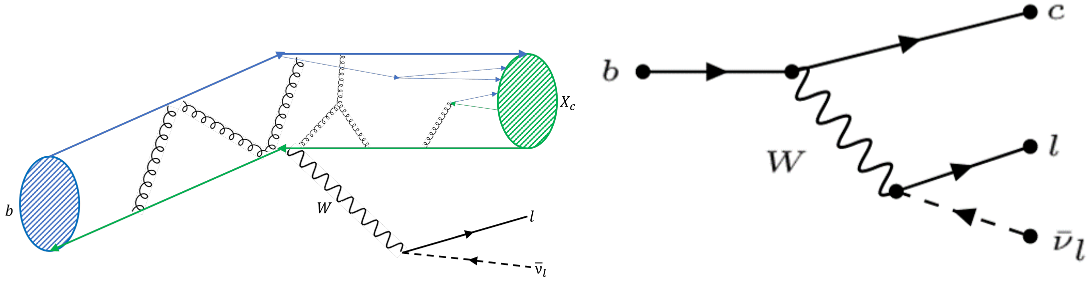

Figure 4: Feynman Diagram for the inclusive $b \to c l \bar{\nu}_l X$ decay (left) and exclusive $B \to X_c l \bar{\nu}_l$ decay (right).

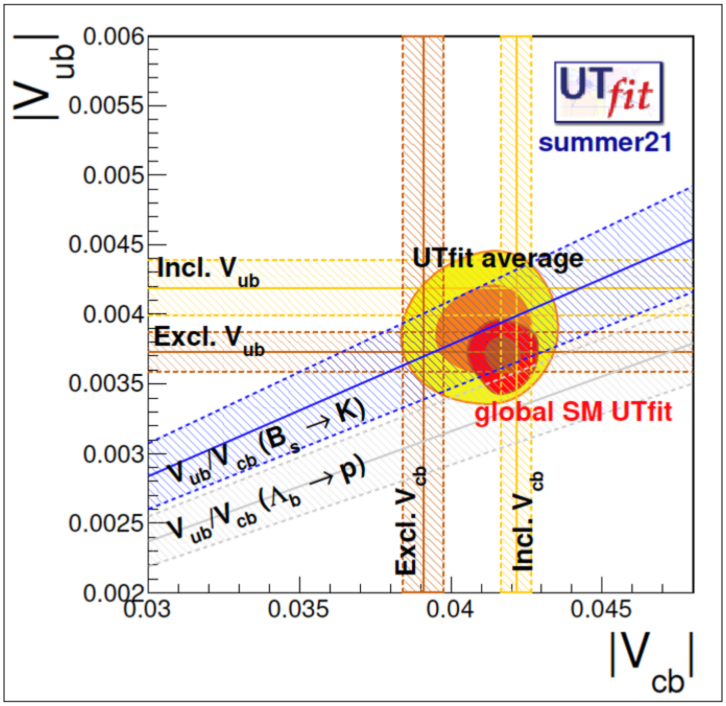

Figure 5: Current UT Fit [3] of the CKM parameters $|V_{ub}|$ and $|V_{cb}|$, showing the discrepancy between inclusive and exclusive measurements.

channels are useful for probing CKM elements, as they involve only a single hadronic current, which can be parameterized by scalar functions known as form factors. Heavy Quark Effective Theory (HQET) [7] offers a technique to include nonperturbative corrections for decays involving hadrons with a heavy quark, simplifying QCD matrix element calculations. The Λ_b baryon is particularly attractive in HQET, as the light ud pair has a total spin j=0, and is therefore unaffected by chromomagnetic corrections, which are of the order of a few percent in B-meson decays.

HQET was made possible by Isgur and Wise [8], who discovered the flavor and spin symmetries of QCD in the limit of infinitely heavy quark masses. Since the b and c quarks are heavier than the scale of the QCD coupling constant, these symmetries can be exploited, correcting for the finite quark masses through a series expansion with terms $\propto 1/m_{b,c}$. The decay $\mathit{\Lambda}_b^0 \rightarrow \mathit{\Lambda}_c^+ \mu \overline{\nu}_\mu$ (Fig. 6) is parameterized by six independent form factors in HQET. To first order in $1/m_b$, these six scalar functions can all be described in terms of a single function, the Isgur-Wise (IW) function $\zeta(w)$, where w is $v_{\Lambda_b} \cdot v_{\Lambda_c}$, the scalar product of the 4-velocities of the initial and final state baryons in the decay.

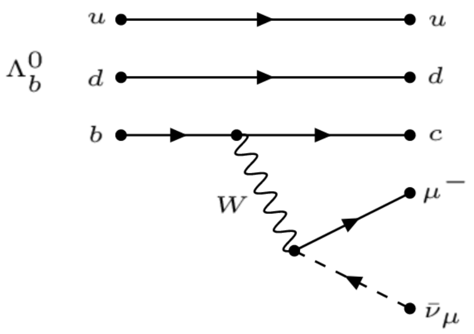

Figure 6: Feynman diagram for the decay $\Lambda_b \rightarrow \Lambda_c \mu \overline{\nu_\mu}$

Lattice QCD calculations are used to calculate the six form factors described by the IW function in terms of q^2 [9], which is the invariant mass of the $\mu - \nu_\mu$ pair, for the decay $\Lambda_b \to \Lambda_c \mu \overline{\nu}_\mu$. The relationship between w and q^2 is

$$w = (m_{\Lambda_b}^2 + m_{\Lambda_c}^2 - q^2)/2m_{\Lambda_b} m_{\Lambda_c} \tag{5}$$

A measurement of the shape of the differential decay rate, $d\Gamma/dq^2(\Lambda_b \to \Lambda_c \mu \overline{\nu}_\mu)$ was performed [10] to compare the consistency of the lattice calculations with data collected by the LHCb experiment. This work expands on the results obtained in [10] by deriving the absolute value of $\Gamma(\mathit{\Lambda}_b^0 \to \mathit{\Lambda}_c^+ \mu^- \overline{\nu}_\mu)$ and comparing this measured value with Lattice QCD predictions to extract a measurement of $|V_{cb}|$. Additionally, the analysis method presented will allow for the first precise determination of the absolute branching fraction $\mathcal{B}(\Lambda_b \to \Lambda_c \mu \overline{\nu}_\mu)$.

2 The LHCb Experiment

2.1 Introduction

The Large Hadron Collider - Beauty (LHCb) detector, figure 7, is designed to study the b-quark and it's decays. It is one of the primary experiments constructed at the Large Hadron Collider (LHC), a 27km proton-proton collider located at CERN in Geneva. The LHC was operated in Run 2 between 2015 and 2018, and achieved a luminosity of $2 \times 10^{34} cm^{-2} s^{-1}$ with a collision energy $\sqrt{s} = 13$TeV [11]. To reach this luminosity, bunches of protons are sent in opposite directions around the LHC. Proton bunches, each containing about 1.2×10^{11} protons and separated by 25ns, and are forced to collide at one of four points in the LHC, illustrated in figure 8.

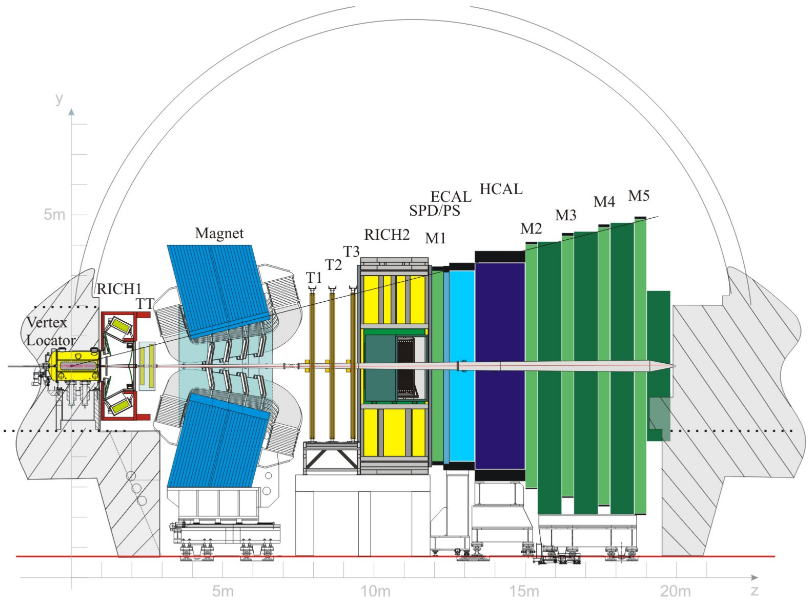

Figure 7: Side view of the LHCb detector.

The LHC produces $b\bar{b}$ pairs with a cross section $\sigma = 144 \pm 1 \pm 21 \mu b$ at 13TeV. The large number of $b\bar{b}$ pairs hadronize into B mesons and long-lived Λ_b baryons, which allow for precision measurements of CKM parameters, searches for rare B decays, and investigations of CP-violating processes, all of which could shed light into new physical processes.

In the LHC, $b\bar{b}$ pairs are created by the strong interaction via proton-proton collisions. Because the energy of the pp collision is much higher than that of the $b\bar{b}$ invariant mass, the $b\bar{b}$ pairs are boosted in the direction of the highest energy parton involved in the collision. This corresponds to mostly low-angles with respect to the beam direction, as shown in figure 9. To exploit the mostly forward production of b-quarks in

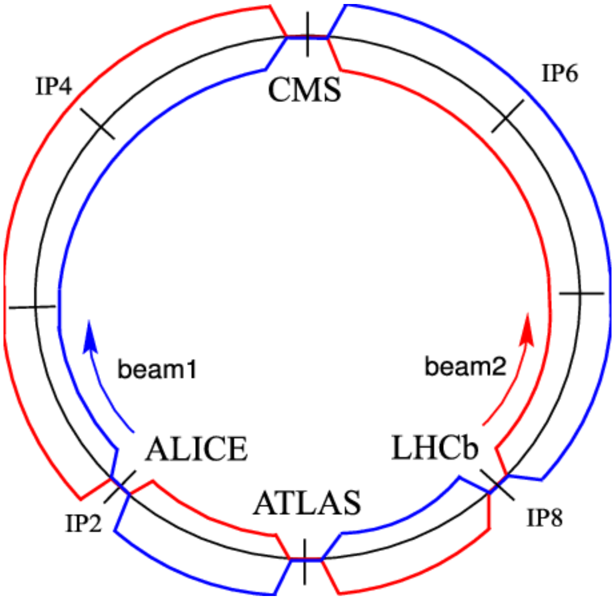

Figure 8: Schematic layout of the LHC showing the four interaction points.

the LHC, the LHCb detector is designed and constructed as a single-arm forward spectrometer, covering a pseudorapidity (η) range of $2 < \eta < 5$, where η is defined as $-ln(tan\frac{\theta}{2})$, and θ is the polar angle with respect to the beam axis.

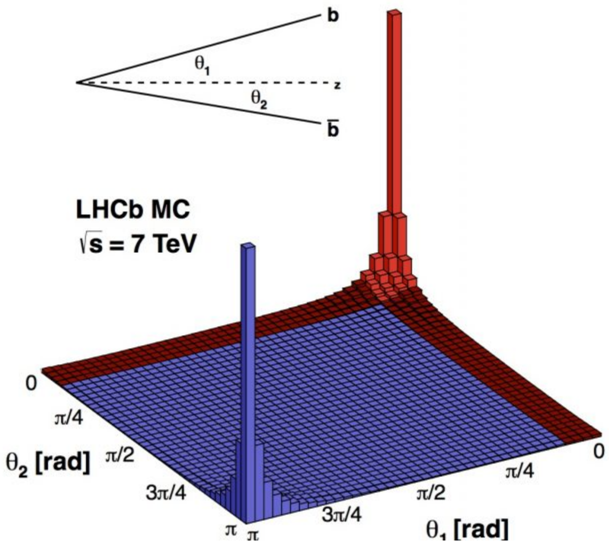

Figure 9: Angular correlation of b-quarks seen in LHCb originating from proton-proton collisions.

The LHCb consists of several subdetectors: the Vertex Locator (VELO), two Ring-Imaging Cherenkov

Detectors (RICH1 and RICH2), the Tracking Stations (TT, T1, T2, T3), Electromagnetic and Hadronic Calorimeters (ECal and HCal), and five Muon tracking stations (M1 to M5). The subdetectors are separated by the dipole magent used to bend charged tracks to resolve their momenta.

2.2 Tracking

2.2.1 Vertex Locator

The Vertex Locator (VELO) [12] is used to precisely measure the location of the primary vertex (PV) of a decay and to measure the impact parameter of all tracks relative to the PV, and thus obtain precision measurements of $b-$ and $c-$quark decay vertex positions and lifetime measurements. To accomplish this, the VELO makes use of 42 silicon modules, each made from two $300\mu m$ thick silicon half-discs with either radial or polar oriented strips. The modules are arranged with cylindrical geometry, closing to a distance of about $7mm$ around the interaction point. A schematic representation of the VELO modules and geometry is showin in figure 10. In this configuration, most B-hadrons decay within the VELO volume and the primary vertex can be reconstructed using tracks coming directly from the interaction point. Sufficiently displaced tracks are then used to reconstruct the secondary vertex with high accuracy.

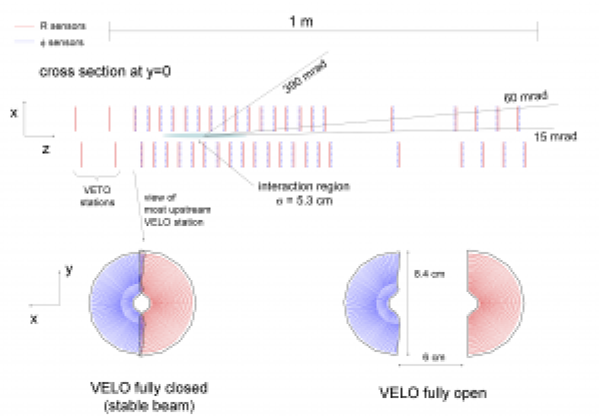

Figure 10: Schematic view of the VELO detector showing the module layout in the $x-z$ plane (top), and the VELO sensors in either their fully-closed or fully-open configurations (bottom).

Because the VELO detector is situated very close to the beam-line, the components are subject to the highest doses of radiation from the proton beam. To help prevent damage, each of the two VELO are mounted on custom built bellows. The bellows allow each detector half to be withdrawn away from the beam line during times when the beam may be unstable.

2.2.2 Tracking Stations

In addition to the VELO, four tracking stations are used to reconstruct the flight path of a charged particle through the detector. These stations are the Tracker Turicensis (TT), located just upstream of the dipole magnet, and the three downstream tracking stations T1, T2, and T3 [13]. Each of the downstream stations are further divided into two subdetectors: the Inner Tracker (IT) which is a cross-shaped region that lies close to the beam pipe, and the Outer Tracker (OT), which covers the remaining acceptance of the LHCb further away from the beam pipe. The geometry of the TT, IT, and OT can be seen in figure 11.

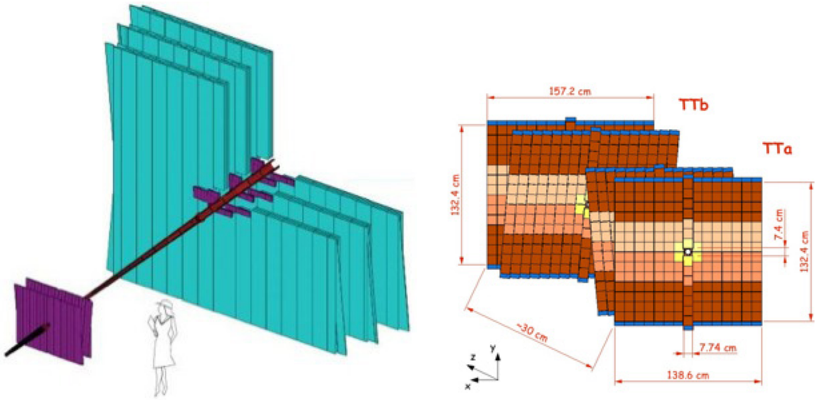

Figure 11: Geometry of the IT (purple) and OT (teal). The IT consists of the TT, and the inner region of the T-stations (left). The TT (right) is comprised of four silicon module layers. The two inner layers are oriented at either +5° or −5° around the beam axis.

The tracking system employs two different module species to detect passing particles. Because of the large particle density in the TT and IT detectors, modules are made using silicon microstrip detectors, each with readout strips with about $200\mu m$ pitch and a spatial resolution of around $50\mu m$ ($57\mu m$) in the TT (IT). To detect a passing track, an electric field is established within the silicon sensor. As a charged track passes through the sensor bulk, charge carriers are liberated and travel to the implanted strips via the field. The signal is collected and amplified by dedicated read-out electronics, and the position of the track is registered.

The TT and IT detectors, together called the Silicon Tracker (ST), are made from four layers of silicon modules: two layers have sensors with strips oriented vertically, and two are arranged such that the strips are rotated by +5° and −5° around the direction of the beam in order to maximize momentum resolution. In LHCb, most tracks are produced in the forward direction, and therefore the ST sees about 20% of the total number of tracks in the detector, despite only covering about 2% of the sensitive area.

While silicon modules offer very fine spatial resolution, their cost make them impractical for covering large areas. The OT covers the remaining 98% of the detector acceptance, and is constructed form 72 separate modules made from straw-tube drift chambers. The modules are made of a gas-tight box containing 256 tubes filled with $Ar - CO_2$ drift gas. Tubes are arranged in staggered layers, and are made from an inner layer of carbon-doped Kapton which acts as a cathode. As a track ionizes the gas, electrons are knocked out of their energy shells and are collected by front-end electronics.

2.2.3 Muon System

The muon detector system [14] is used to identify and track muons in LHCb, and plays a vital for many physics analyses, like searches for rare decays such as $B_s \to \mu\mu$. In semileptonics, the presence of a muon is of particular importance to tag the flavor of the neutral parent B hadron. The muon system also provides key information to the earliest Level-0 trigger stage. Information must be gathered within 20ns, and thus the muon system is optimized for speed. The detector also provides identification information to the HLT software trigger.

The muon system is comprised of five stations M1 to M5. The first station, M1, sits before the calorimeters, and is primarily used for high-PT muon triggering. The remaining stations, M2 through M5, are placed after the calorimeter system. Each layer downstream of the calorimeter is separated by iron filters, used to stop hadrons exiting the HCAL so that only muons are detected. The muon system, illustrated in figure 12, is divided into four regions with increasing distance from the beam axis. The total coverage of the muon system is $435m^2$, covering $\pm 300mrad$ in the horizontal plane and $\pm 250mrad$ in the vertical direction, with varying granularity so that the occupancy of the detector remains constant. The granularity is optimized in the horizontal plane to provide more accurate measurements of p_T and track momentum.

The five stations are filled with CO_2, Argon, or Tetrafluoromethane gas, in which a passing muon will ionize and the resulting signals are detected by wire electrodes. The muon system houses about 1400 Multi-Wire Proportional Chambers (MWPC), save for the inner part of M1 which uses triple-GEM (Gas Electron Multipliers) to cope with the high particle rate in this region.

Passing tracks are tagged as muons if they correspond to a certain number of hits observed in the five muon stations, depending on the track's momentum. Hits in a station are associated to a track if it is found within a spatial Field of Interest (FOI), which is a function of the track momentum and the extrapolated track within the muon chambers. For tracks that pass these requirements, summarized in table 2, a hypothesis test is preformed to evaluate the consistency of each track with the yes/no hypothesis that the track is a muon. A delta log-likelihood is constructed from these two hypotheses, and this information is combined with information from the RICH detectors to provide a global PIDmu likelihood variable.

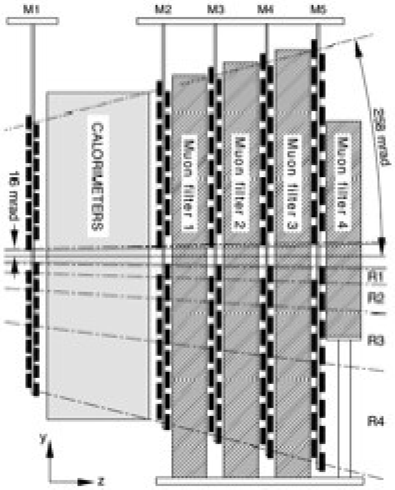

Figure 12: Layout of the five muon stations M1 through M5.

Table 2: Muon detector stations required to provide a positive muon trigger decision as a function of track momentum.

$\overrightarrow{p}_{Trk}$[GeV]	Required Muon Stations
$3 < \overrightarrow{p}_{Trk} < 6$	M2+M3
$6 < \overrightarrow{p}_{Trk} < 10$	M2+M3+(M4||M5)
$\overrightarrow{p}_{Trk} > 10$	M2+M3+M4+M5

2.3 Dipole Magnet

To measure the momentum of charged tracks in an event, powerful magnets are used to bend the flight path of particles that nominally fly in straight lines. In LHCb, tracking stations must provide a momentum measurement with about 0.4% precision for track momenta up to 200GeV/c. The LHCb detector employs a dipole magnet [15], shown in figure 13, which consists of two warm, horseshoe shaped magnets that produces an integrated field of $4T \cdot m$. During operation, the polarity of the magnet is alternated to improve systematic uncertainties.

2.4 Particle Identification (PID)

Given the high luminosity seen in the LHCb detector, it becomes a challenging task to separate signal events from various background sources. One tool to help separate signal from background is a robust method to associate tracks in an event as coming from a particular species of particle. Differentiating kaon tracks from pion tracks, for example, can greatly reduce backgrounds in a data sample by helping to isolate events

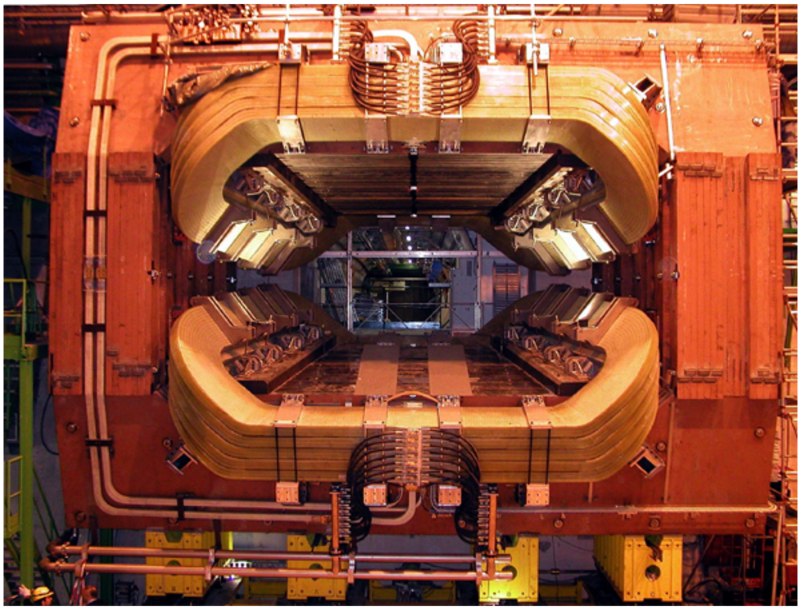

Figure 13: The LHCb Dipole Magnet viewed looking upstream in the experimental area.

coming from the specific decay of interest. The LHCb detector is equipped with several subdetectors used to associate a track with a particle species. In addition to the muon identification provided by the muon stations, LHCb uses two Ring Imaging Cherenkov Detectors: RICH1, RICH2, as well as Electromagnetic and Hadronic Calorimeters (ECAL & HCAL).

2.4.1 RICH1 and RICH2

The RICH1 and RICH2 [16] subdetectors are used in conjunction with the tracking system to identify charged tracks. A charged particle that travels faster than the local speed of light in a medium will emit Cherenkov radiation in the form of cones of light. The angle of the emitted light cone is proportional to the track's velocity. Inside of the RICH detectors, these light cones are focused onto Hybrid Photo Detectors (HPD) through the use of both spherical and flat mirrors. The focused light cones are projected as rings onto the HPDs, and the size and shape of the ring corresponds to speed of the track. This measurement, combined with the measured track momentum from the tracking system, gives knowledge of the mass of the particle corresponding to the track, and thus the species of particle is known.

The RICH1 detector is located just after the VELO system and covers the full LHCb acceptance. Tracks with relatively low momentum, on the order of a few GeV, are identified via the silica aerogel Cherenkov medium. Tracks with higher momentum, from around 10GeV/c to 65GeV/c, are identified via the C_4F_{10} gas radiator in RICH1.

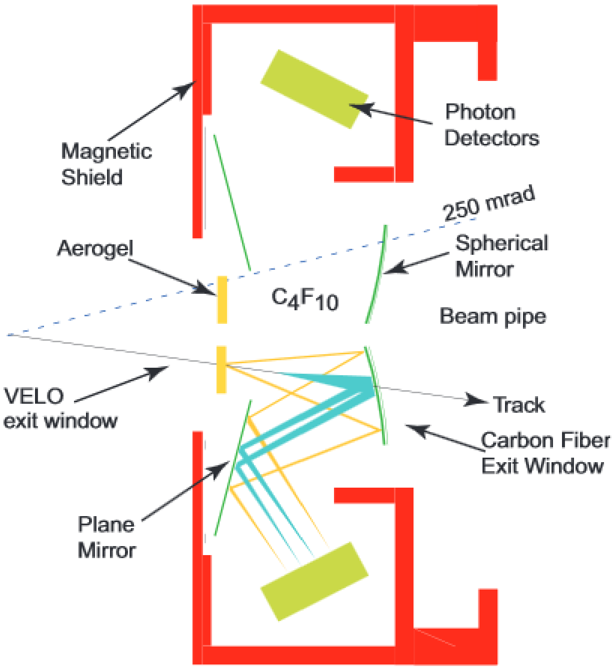

Figure 14: Schematic view of the RICH1 detector. RICH2 is constructed similarly, with a different Cherenkov radiator and mirror material.

RICH2 is situated behind the magnet and tracking system. It uses CF_4 as a radiator. It is designed to measure mostly high-momentum tracks, up to 100GeV/c, and therefore only covers a limited acceptance region. A schematic representation of the RICH detector is shown in figure 14. Together, the RICH system identifies charged tracks combing from B decays, such as protons, Kaons, and pions. The images collected by both RICH1 and RICH2 are compared with the patters expected from hypothesized particles, and a likelihood is calculated from this comparison.

2.4.2 Calorimeters

The LHCb Calorimeter system [17] is used to identify on electrons, photons, and neutral hadrons, and to provide energy and position measurements of downstream tracks used in the trigger. The calorimeter system in LHCb consists of the Scintillating Pad Detector and Preshower (SPD/PS), the Electromagnetic Calorimeter (ECAL), and the Hadronic Calorimeter (HCAL). Each detector has a similar construction, with alternating metal layers used to stop particles, and plastic layers used to measure energy from the resulting particle shower.

The first stage of the calorimeter system is the SPD and PS detectors. The SPD provides information on whether the incident particle is charged or neutral, and the PS is used to determine the electromagnetic signature of the particle. The SPD/PS are constructed from two 15mm thick scintillating pads, separated by a $2.5X_0$ lead layer to separate electrons from photons. When a passing particle ionizes a scintillator, the absorbed energy is emitted as light, which is then carried by wavelength-shifting (WLS) fibers to standard Photo Multiplier Tubes (PMT) located at either end of the fibers. The resulting signal is then used in conjunction with the ECAL to trigger events based on the presence of electrons, photons, or neutral π^0 mesons.

Similarly, the ECAL is constructed by alternating layers of lead and scintillating tiles. It is comprised of three different module types with cell sizes of $4 \times 4cm$ in the innermost part of the detector, $6 \times 6cm$ for the middle layers, and $12 \times 12cm$ for the outermost part. The varying cell sizes account for differing occupancy levels in different regions of the detector acceptance, and correspond to the granularity of the SPD/PS for use in separating photons and electrons. The energy resolution of the ECAL is:

$$\frac{\sigma(E)}{E} = \frac{10\%}{\sqrt{E}} \oplus 1\% \tag{6}$$

where E is the hadron energy in GeV.

The HCAL sits just behind the ECAL, and is comprised of iron layers separated by scintillating modules lying parallel to the beam line. The HCAL also features modules with two different cell sizes, $13 \times 13cm$ for the inner region and $26 \times 26cm$ in the outer part of the detector. The segmentation of modules for both the ECAL and HCAL can be seen in figure 15. In the transverse direction, the scintillating tiles are inter spaced with $1cm$ iron layers to match the radiation length X_0. Parallel to the beam axis, scintillators and iron layers are spaced according to the interaction length λ_1 in iron, as shown in figure 16. Due to spatial constraints in the LHCb cavern, the size of the HCAL is limited and hadronic showers are not always fully absorbed by the calorimeter. The Energy resolution of the HCAL is:

$$\frac{\sigma(E)}{E} = \frac{(69 \pm 5)\%}{\sqrt{E}} \oplus (9 \pm 2)\% \tag{7}$$

The subdetectors of the Calorimeter system work in conjunction to reconstruct photons, electrons, and neutral hadrons. Photons are identified as neutral clusters observed in the ECAL, which are not associated with any reconstructed tracks. Neutral pions can be reconstructed either by resolving two well separated photons within the ECAL. For π^0 particles with high transverse momentum, the two photons can not be well resolved as separate clusters, and so iterative techniques are used to reconstruct the pion from a single

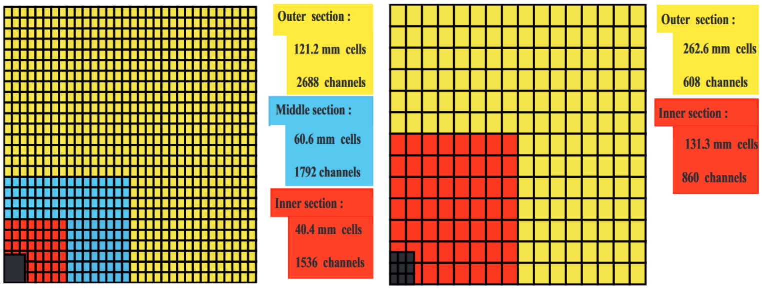

Figure 15: Segmentation of modules in the ECAL (left) and HCAL (right). The dark region in the bottom left corners represent areas occupied by the beam pipe.

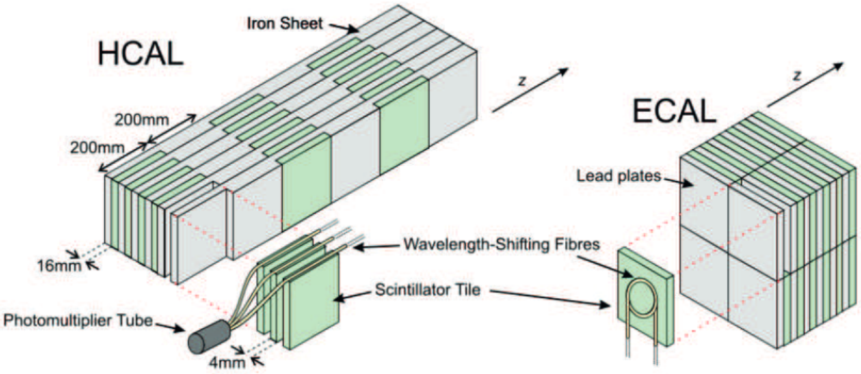

Figure 16: Illustration of the construction of scintillating modules and metal filters in the HCAL (left) and ECAL (right).

merged cluster in the ECAL. More information can be found in [18].

2.5 Trigger

Due to the immense amount of events produced in the proton-proton collisions during the LHC operation, a sophisticated system is required to efficiently select interesting B events from the vast amount of uninteresting background. The LHCb trigger system [19] is designed with this goal in mind. The two stage system is made up of the Level-0 (L0) hardware trigger, and the software High Level Trigger (HLT) system. The trigger stages work to reduce the event rate from 40MHz down to a few kHz, which is then written to offline storage.

2.5.1 Level-0 Trigger

The first trigger stage is the L0 trigger, which reduces the data rate from 40MHz to 1MHz, is a fully hardware trigger that is built from custom electronics with a $4\mu s$ fixed latency. L0 accomplishes this by exploiting tracks with large transverse momentum using information collected by the Calorimeter, Muon, and VELO subdetectors. It is divided into the three following components:

- **The L0Calo Trigger:** L0 collects information from the SPD/PS, ECAL, and HCAL to find and select clusters from neutral hadrons, electrons, and photons. A measurement of the transverse energy is performed, where E_T is defined as:

  $$E_T = E_0 cos\theta \tag{8}$$

  where E_0 is the incident energy seen from the hit in a particular module, and θ is the polar angle of the track. Fast selections are made based on E_T criteria and candidates are stored according to L0Hadron, L0Electron, and L0Photon lines. The number of hits recorded in the SPD also provides a fast, hardware based determination of the charged-track multiplicity of an event.

- **The L0 Muon Trigger:** Hits in all five muon stations are required for a candidate to trigger either the L0Muon or L0DiMuon lines. The L0 muon electronics select the two tracks with the highest p_T in each quadrant of the Muon detector. A lower threshold on the highest-p_T track is set by the L0Muon trigger, or, a threshold on the product of the largest and second-largest p_T tracks is set by the L0DiMuon trigger. Events with high track multiplicity, as recorded by the SPD, are vetoed, and a total output rate of 1MHz is passed to the HLT1 stage.

- **The L0 Pile-Up Trigger:** Two modules upstream of the VELO provide track multiplicity information to L0 for the Beam-Gas Trigger decision. Protons can interact with residual gas molecules left in the vacuum tube. If a beam-gas event is triggered by the proton beam originating upstream of the magnet, signals in the calorimeters are expected in addition to the Pile-Up modules. Beam-gas events triggered by the opposing beam are expected only in the pile-up modules, and thus events can be rejected or accepted based on the calorimeter activity for beam-gas triggered events coming from either beam. The beam-gas events also are used in luminosity measurements.

2.5.2 Hlt1 Trigger

The High Level Trigger divided into two stages, Hlt1 and Hlt2. The first stage, Hlt1, is used to provide a first estimate of the primary vertex location. Events sent by the L0 trigger are passed to HLT1 at a rate of

1MHz, and is reduced to around $110kHz$. The Hlt1 trigger uses several lines operating in parallel:

- **The Inclusive Trigger:** Information provided by the VELO and tracking detectors is used to look for events with $p_T > 500$MeV and a high impact parameter with respect to the pp vertex. Long lived B candidates will fly for about $1cm$ before decaying, and thus provide a good signature for the candidate decaying in the VELO. At least three additional hits in the TT are required around a straight-line extrapolation from the VELO tracks. Finally, tracks are extrapolated to the T-stations, and all tracks are fit with a Kalman filter. VELO tracks are also re-used to estimate the PV location. The inclusive lines select events in which either a single, high p_T track is displaced from the PV, or a displaced two-track vertex is seen.

- **The HLT1 Muon Trigger:** If an event is triggered by one of the L0Muon lines, tracks reconstructed in the VELO are extrapolated and matched with those from the Muon stations that provided the L0 trigger decision. Four main lines are used to select *a*) a single displaced muon with high p_T, *b*) a muon with very high p_T without displacement, *c*) a di-umon pair originating from a *c*- or *b*-quark decay, or *d*) displaced di-muon pairs with no mass requirement.

- **Hlt1 electron and photon triggers** use information from the ECAL to veto events based on their energy signatures.

2.5.3 HLT2 Trigger

The Hlt2 is the second software trigger stage, and reduces the total event rate to a few kHz which is written to offline storage. Hlt2 uses the Hlt1 output, in addition to information from all the subdetectors, to fully reconstruct the event by *a*) reconstructing charged tracks, *b*) reconstructing neutral tracks, and *c*) apply particle identification. Hlt2 can also reconstruct tracks utilizing techniques unavailable to Hlt1 in order to, for example, reduce inefficiencies from the TT acceptance, or to reconstruct long-lived particles from tracks that decay outside the VELO.

High multiplicity events, which would require long processing times, are rejected via Global Event Cuts (GEC), which veto events based on measured values such as the total number of reconstructed tracks. In the Hlt2 stage, the full event reconstruction allows for a wide range of possible final states to be selected by dedicated HLT2 lines. Inclusive trigger lines look for events with either well displaced two-, three-, or four-body decays with topologies consistent with *b*-decays.

As understanding of the trigger system evolved after Run1, an improved trigger strategy was implemented in Run2. The *Real-Time Analysis* (RTA) method stages events processed by Hlt1 onto disk storage. Thus,

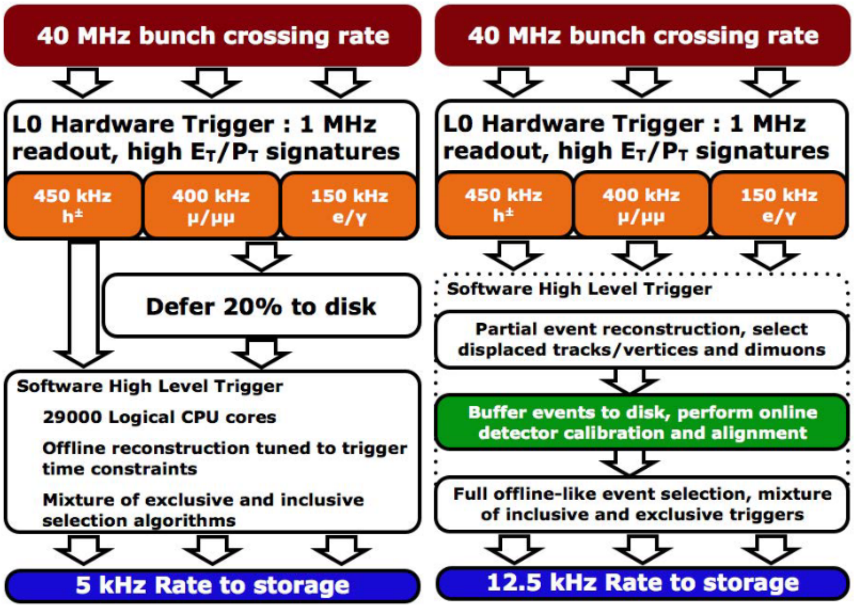

Figure 17: Trigger strategy used in LHCb during Run1 (left) and Run2 (right).

further event processing became possible during inter-fill periods, and detector alignment could be performed in real-time on a run-by-run basis, before events were sent to Hlt2. A comparison of the trigger strategy employed in Run1 and Run2, with the optimized output rates, is shown in figure 17.

3 Analysis Method

A method of extracting a preliminary measurement of $|V_{cb}|$ in the decay $\Lambda_b^0 \to \Lambda_c^+ \mu^- \overline{\nu}_\mu$ is presented. For the rest of this study, charge conjugation is implied. Data from pp collisions with a center-of-mass energy of 13TeV, collected by the LHCb detector in 2017, is used to study the decays $\Lambda_b \to X_c \mu \overline{\nu}_\mu$, where X_c represents a charmed baryon, with the goal of isolating the final state $\mathit{\Lambda}_b^0 \to \mathit{\Lambda}_c^+ \mu^- \overline{\nu}_\mu$ and determine the CKM parameter $|V_{cb}|$. The inclusive $\Lambda_b \to \Lambda_c \mu \overline{\nu}_\mu X$ decays are identified by reconstructing a μ together with a Λ_c originating from a common vertex. The Λ_c is found by reconstructing proton, kaon, and pion tracks pointing to a common vertex.

Raw yields for the ground state $\Lambda_b \to \Lambda_c \mu^- \overline{\nu}_\mu$ are determined via a fit to the corrected mass, defined as

$$m_{corr} = \sqrt{m^2_{\Lambda_c \mu} + p^2_{T,\Lambda_c \mu}} + p_{T,\Lambda_c \mu} \tag{9}$$

The fit includes template shapes to account for contributions from the higher mass $\Lambda_b \to \Lambda_c^* \mu \overline{\nu}_\mu$ other background channels. The total yield is then corrected for detector efficiencies and other factors, such as inconsistencies in particle identification and trigger output between data and simulation. A subsequent scaling factor accounting for the branching fraction $\mathcal{B}(\Lambda_c^+ \to pK^-\pi^+)$ is applied, and thus the total corrected yield for the ground state decay $N_{corr}(\mathit{\Lambda}_b^0 \to \mathit{\Lambda}_c^+ \mu^- \overline{\nu}_\mu)$ is obtained.

In order to extract the total semileptonic width, the method presented in [20] is used to normalize the corrected yield to the inclusive semileptonic branching fraction $\mathcal{B}(\Lambda_b \to X_c \mu \overline{\nu}_\mu)$. This relies on determining the total number of $\mathit{\Lambda}_b^0 \to \mathit{\Lambda}_c^+ \mu^- \overline{\nu}_\mu X$ events, as well as contributions from $\mathit{\Lambda}_b^0 \to D^0 p \mu^- \overline{\nu}_\mu$ and $\Lambda_b \to D^+ n \mu^- \overline{\nu}_\mu$ decays, in order to determine $N_{corr}(\Lambda_b \to X_c \mu \overline{\nu}_\mu)$. In this method, the equality of semileptonic widths in different b-flavored hadrons is exploited, which is correct to order $1/m_b^2$ in HQET. A small correction factor accounts for the absence of chromomagnetic effects in Λ_b decays, which is estimated as $(3 \pm 1.5)\%$, and a more precise estimate is imminent. Therefore, the inclusive semileptonic width $\Gamma(\Lambda_b^0 \to X_c \mu^- \overline{\nu}_\mu)$ can be obtained from the inclusive B semileptonic branching fractions, which have been well measured at the b-factories. The b-hadron branching fractions and lifetimes used in this analysis are summarized in table 3. Using this assumption, the inclusive semileptonic width of a Λ_b^0 baryon decaying to a charm hadron, plus a $\mu \overline{\nu}_\mu$ pair, is given by

$$\Gamma(\mathit{\Lambda}_b^0 \to X_c \mu^- \overline{\nu}_\mu) = \mathcal{B}(B \to X_c \mu^- \overline{\nu}_\mu) \cdot \tau_B \cdot \xi \tag{10}$$

where $\mathcal{B}(B \to X_c \mu^- \overline{\nu}_\mu)$ is the inclusive semileptonic branching fraction for $B \to X_c l \overline{\nu}_l$ shown in tab. 3, τ_B is the average lifetime of the lighter B mesons, and ξ is the chromomagnetic correction factor.

Table 3: Measured semileptonic decay branching fractions for B mesons and derived branching fractions for B_s and $\mathit{\Lambda}_b^0$ based on the equality of semileptonic widths and the lifetime ratios [4] [5].

Particle	τ (ps) measured	$\mathcal{B}_{\mathrm{SL}}$ (%) measured	Correction [5]	$\mathcal{B}_{\mathrm{SL}}$ (%) to be used
$\overline{B}^0$	1.520 ± 0.004	10.30 ± 0.19		10.30 ± 0.19
B^-	1.638 ± 0.004	11.08 ± 0.20		11.08 ± 0.20
$\left\langle \overline{B}^0 + B^- \right\rangle$		10.70 ± 0.19		10.70 ± 0.19
$\overline{B}_s^0$	1.526 ± 0.015		(-1.0±0.5)%	10.22 ± 0.56
$\mathit{\Lambda}_b^0$	1.470 ± 0.010		(3.0±1.5)%	10.24 ± 0.25

The corrected Λ_b^0 inclusive yield is determined from the method presented in Ref [20]:

$$n_{\mathrm{corr}}(\mathit{\Lambda}_b^0 \to X_c\mu) = \frac{n(\mathit{\Lambda}_c^+\mu^-)}{\mathcal{B}(\mathit{\Lambda}_c^+ \to pK^-\pi^+)\epsilon(\mathit{\Lambda}_b^0 \to \mathit{\Lambda}_c^+)} + \kappa\frac{n(D^0 p\mu^-)}{\mathcal{B}(D^0 \to K^-\pi^+)\epsilon(\mathit{\Lambda}_b^0 \to D^0 p)}, \tag{11}$$

where the X_c represents a generic charm hadron. Here, the shorthand $n(\mathit{\Lambda}_c^+\mu^-)$ represents the yield for a final state $\Lambda_b^0 \to \mathit{\Lambda}_c^+\mu^-\overline{\nu}_\mu X$, which includes contributions from the ground state $\Lambda_b^0 \to \Lambda_c^+\mu^-\overline{\nu}_\mu$ decay, as well as $\Lambda_b^0 \to \Lambda_c^{*+}\mu^-\overline{\nu}_\mu$ decays. The second term accounts for the cross feed channel $\Lambda_b^0 \to D^0 p\mu^-\overline{\nu}_\mu X$. The factor κ is set to 2 to account for $\Lambda_b^0 \to D^+ n\mu^-\overline{\nu}_\mu X$ final states.

The corrected exclusive yield $N_{corr}(\Lambda_b^0 \to \Lambda_c^+\mu^-\overline{\nu}_\mu)$, together with the inclusive semileptonic yield determined by equation 3, is then used to extract the exclusive semileptonic width. Using

$$\frac{N_{corr}(\Lambda_b^0 \to \Lambda_c^+\mu^-\overline{\nu}_\mu)}{N_{corr}(\Lambda_b^0 \to X_c^+\mu^-\overline{\nu}_\mu)} = \frac{\Gamma(\Lambda_b^0 \to \Lambda_c^+\mu^-\overline{\nu}_\mu)}{\Lambda_b^0 \to X_c^+\mu^-\overline{\nu}_\mu}, \tag{12}$$

the exclusive semileptonic can be determined by

$$\Gamma(\Lambda_b^0 \to \Lambda_c^+\mu^-\overline{\nu}_\mu) = \frac{N_{corr}(\Lambda_b^0 \to \Lambda_c^+\mu^-\overline{\nu}_\mu)}{N_{corr}(\Lambda_b^0 \to X_c^+\mu^-\overline{\nu}_\mu)} \times \Gamma(\Lambda_b^0 \to X_c^+\mu^-\overline{\nu}_\mu) \tag{13}$$

A theoretical estimate of $\Gamma(\mathit{\Lambda}_b^0 \to \mathit{\Lambda}_c^+\mu^-\overline{\nu}_\mu)/|V_{cb}|^2$ has been presented by Ref. [9]. The ratio between the experimental $\Gamma(\Lambda_b^0 \to \Lambda_c^+\mu^-\overline{\nu}_\mu)$ and this theoretical prediction gives an experimental evaluation of $|V_{cb}|^2$. The following sections describe the data sample used to derive the measured $N_{raw}(\mathit{\Lambda}_b^0 \to \mathit{\Lambda}_c^+\mu^-\overline{\nu}_\mu)$, and the correction factors applied to determine $N_{corr}(\mathit{\Lambda}_b^0 \to \mathit{\Lambda}_c^+\mu^-\overline{\nu}_\mu)$. The comparison of the measured spectrum with lattice predictions is discussed in the final chapter.

3.1 Event Selection

The data set used in this analysis was collected by the LHCb experiment in 2017, corresponding to a total luminosity of $1.71 fb^{-1}$. Triggered events are subject to the so-called *Stripping* algorithm, which sets the criteria for which events are stored to disk. The selections pertaining to the samples used in this analysis come from one of two dedicated semileptonic lines, $StrippingB2DMuNuX\_Lc$ or $StrippingB2DMuNuX\_D0$, for $\Lambda_b \rightarrow \Lambda_c \mu \overline{\nu}$ or $\Lambda_b \rightarrow D^0 p \mu \overline{\nu}$ events respectively. The selections for either line are similar, and are summarized in table 4.

Table 4: Stripping criteria for version 29r2 of the LHCb Stripping project. Proton selections apply only to the *StrippingB2DMuNuX_Lc* line; all other selections apply to both *StrippingB2DMuNuX_Lc* and *StrippingB2DMuNuX_D0* lines.

Global Event	Requirement
nLongTracks	> 250
n Primary Vetex	≥ 1
Muon	Requirement
p_T	$> 1000MeV$
p	$> 6000MeV$
$\chi^2_{Trk.}/n.d.f.$	< 3
$Track\ Ghost\ Prob.$	< 0.35
$\chi^2_{IP,\ PV}$	> 9
PID_{mu}	> 0
Proton	Requirement
p_T	$> 250MeV$
p	$> 8000MeV$
$\chi^2_{Trk}/n.d.f.$	< 3
$Track\ Ghost\ Prob.$	< 0.35
$\chi^2_{IP,\ PV}$	> 4
PID_p	> 0
$PID_p - PID_K$	> 0
Kaon	Requirement
p_T	$> 250MeV$
p	$> 2000MeV$
$\chi^2_{Trk.}/n.d.f.$	< 3
$Track\ Ghost\ Prob.$	< 0.35
$\chi^2_{IP,\ PV}$	> 4
PID_K	> -2
Pion	Requirement
p_T	$> 250MeV$
p	$> 2000MeV$
$\chi^2_{Trk.}/n.d.f.$	< 3
$Track\ Ghost\ Prob.$	< 0.35
$\chi^2_{IP,\ PV}$	> 4
PID_K	< 10
Charm Hadron	Requirement
$Mass$	$abs(m_{X_c}) < 80MeV$
$\chi^2_{EndVtx.}/n.d.f.$	< 6
$\chi^2_{Vtx.Dist.,BPV}$	> 25
$DIRA$	> 0.99
χ^2_{DOCA}	< 20
Λ_b Candidate	Requirement
$Mass$	$2200MeV < m_{\Lambda_b} < 8000MeV$
$\chi^2_{End\ Vtx.}/n.d.f.$	< 9
$DIRA$	> 0.999
χ^2_{DOCA}	< 10
$z_{S.V.} - z_{P.V.}$	$> -2mm$

3.1.1 Trigger Requirement

Several trigger requirements are applied to the reconstructed particles which comprise the data sample used in this analysis. Candidates are subjected to trigger lines at each of the three trigger levels described in the previous chapter, which provide a decision based on the properties of the events. The trigger decisions are categorized as follows:

- **Triggered On Signal (TOS):** Presence of a signal track(s) in an event results in a positive trigger decision.
- **Triggered Independent of Signal (TIS):** An event generates a positive trigger decision for a line, independent of the presence of the signal candidate.

Muons in the data set are required to have a TOS decision on the L0MuonDecision line. Additionally, muons must be TOS on the Hlt1TrackMuonDecision line, corresponding to an $IP > 0.25mm$ and $\chi^2_{IP} > 16$. Events passing these criteria are subject to the Hlt2 trigger. Several topological lines have been developed to trigger on generic inclusive n-body B decays, whose products include at least two charged tracks. This is accomplished by exploiting properties common to all B decays, and making some modest selections on some or all of the daughters [21]. These lines feature a high signal efficiency and large background rejection factor. For this analysis, the b-candidate must be TOS on any one, or more, of the Hlt2TopoMu(2,3,4)BodyDecision lines, which also require the presence of a muon track in the final state.

3.1.2 Offline Selections

Events that pass the stripping and trigger criteria described above are subject to additional selections based on the decay properties. The Λ_c candidates are constructed with three charged tracks originating from a common vertex, and satisfying particle identification criteria that assign proton, Kaon, and pion identification respectively. The criteria used to select these tracks were adapted from Ref. [10]. Kinematic and track quality constraints are applied the $\mathit{\Lambda}_c^+$ daughters. Furthermore, we include a cut on the IP of the Λ_c candidate to suppress events in which the Λ_c was produced directly from the proton-proton collision (prompt decay), rather than from the decay of a Λ_b baryon.

The reconstructed Λ_c is then combined with a muon track to form the Λ_b candidate. Vertex quality is of particular importance in order to suppress backgrounds coming from combinations with other particles coming from the primary vertex. In addition, our final result will rely on a determination of the $\mathit{\Lambda}_b^0$ momentum, which requires the reconstruction of the $\overline{\nu}_\mu$ four-momentum. To achieve this goal, a well measured secondary vertex location is crucial. All of the selections imposed after the stripping output are summarized in table 5. A similar approach is used to select $\Lambda_b^0 \to D^0 p \mu^- \overline{\nu}_\mu$ events.

Table 5: Offline Selections required of the the $\Lambda_b^0 \to \Lambda_c^+\mu^-\overline{\nu}_\mu$ and $\Lambda_b^0 \to D^0 p\mu^-\overline{\nu}_\mu$ samples. Selections for either channel are similar unless explicitly specified.

Trigger	Requirement
L0MuonDecision	TOS == True
Hlt1TrackMuonDecision	TOS == True
Hlt2TopoMu(2||3||4)BodyDecision	TOS == True
Vertex & Track	Requirement
Λ_c Decay Vertex Quality	$\chi^2/DOF < 6$
Λ_b Decay Vertex Quality	$\chi^2/DOF < 6$
Primary Vertex Quality	$\chi^2/DOF < 9$
Vertex Separation Z	> 0
Muon	Requirement
PID	isMuon & PIDmu > 0
Track $\overrightarrow{p}$	$p_T > 1300MeV \& \overrightarrow{p} > 6000MeV$
NSharedMu	$== 0$
μ Ghost Prob.	< 0.2
Track Quality	$\chi^2_{Trk}/DOF < 3$
χ^2_{IP}	> 9
Pion	Requirement
PID	PIDK < 0& PIDp < 0
Track $\overrightarrow{p}$	$p_T > 300MeV \& \overrightarrow{p} > 2000MeV$
π Ghost Prob.	< 0.2
Track Quality	$\chi^2_{Trk}/DOF < 3$
χ^2_{IP}	> 4
Kaon	Requirement
PID	PIDK > 4
Track $\overrightarrow{p}$	$p_T > 300MeV \& \overrightarrow{p} > 2000MeV$
K Ghost Prob.	< 0.2
Track Quality	$\chi^2_{Trk}/DOF < 3$
χ^2_{IP}	> 4
Proton	Requirement
PID	PIDp > 10& (PIDp-PIDK) > 0
Track $\overrightarrow{p}$	$p_T > 300MeV \& \overrightarrow{p} > 8000MeV$
p Ghost Prob.	< 0.2
Track Quality	$chi^2_{Trk}/DOF < 3$
$p\chi^2_{IP}$	> 4
Charm Hadron	Requirement
Λ_c Flight Dist. Significance	> 100
Average Daug. p_T	$(p_T^p + p_T^K + p_T^\pi)/3 > 700MeV, (\Lambda_b^0 \to \Lambda_c^+\mu^-\overline{\nu}_\mu)$
Average Daug. p_T	$(p_T^K + p_T^\pi)/2 > 600MeV, (\Lambda_b^0 \to D^0 p\mu^-\overline{\nu}_\mu)$
$ln(IP_{PV})$	> -3
Λ_b Candidate	Requirement
$\Lambda_b DIRA$	> 0.999
Pseudorapidity	$2 < \eta < 4.5$
Λ_b Flight Dist.	$> 1.5mm$
Λ_b Flight Dist. Significance	> 200
Λ_b Radius	< 4.8
Additional Selections	Requirement
$p_T^{\Lambda_c\mu}/p_\nu^{CM}$	< 1.1

3.2 Corrections to the $\Lambda_b^0 \to \Lambda_c^+ \mu^- \overline{\nu}_\mu$ Sample

Discrepancies between data and simulation must be corrected for in order to extract the corrected yield $N_{corr}(\Lambda_b^0 \to \Lambda_c^+ \mu^- \overline{\nu}_\mu)$. Corrections are derived both from data-driven techniques and from simulation: the data driven methods are used to determine the efficiency of the trigger strategy and hadron identification, while simulations are used to evaluate the overall efficiency of the offline selections and reconstruction of the final state. Information from each strategy is then used to determine the overall efficiency correction to obtain the corrected exclusive yield.

3.2.1 L0, Hlt1, and Muon ID Efficiency

A data driven method is used simultaneously evaluate the efficiency of correctly identifying a muon, as well as the efficiency of the L0 and Hlt1 trigger requirements listed in table 5. The well-established Tag-and-Probe method [22] is utilizes a calibration sample of $B^+ \to (J/\psi \to \mu^+\mu-)K^+$ decays, which are selected from the *Hlt2PIDB2KJPsiMuMuPosTagged* and *Hlt2PIDB2KJPsiMuMuNegTagged* lines; the selections are detailed in table 6, including additional selections which are specific to this analysis. One muon track in the J/ψ decay is well identified and reconstructed in each sub-detector station (tag), and the second track is subject only to loose selection criteria (probe). The probe track is then sorted into either a *pass* or *fail* category depending on whether it passes the muon ID, L0, and Hlt1 selection criteria. The resulting yields from the fits to the calibration sample is used to determine the efficiency as

$$\varepsilon_{L0,Hlt1,\mu ID} = \frac{N_{pass}}{N_{pass} + N_{fail}} \tag{14}$$

Table 6: Full set of selections, both stripping and offline, applied to the $B^+ \to (J/\psi \to \mu\mu)K^+$ calibration sample.

Probe Muon	Requirement
p_T	$> 1300 MeV$
p	$> 6000 MeV$
$\chi^2_{Trk.}/N.D.F$	< 3.0
χ^2_{IP}	> 9
$InMuonAcceptance$	> 0
Tag Muon	Requirement
p_T	$> 1300 MeV$
p	$> 6000 MeV$
$\chi^2_{Trk.}/N.D.F$	< 3.0
χ^2_{IP}	> 16
PID_μ	> 0
$isMuon$	True
$Track\ Ghost\ Prob.$	< 0.2
$NShared_\mu$	$== 0$
$L0MuonDecision$	$TOS == 1$
$Hlt1TrackMuonDecision$	$TOS == 1$
$InMuonAcceptance$	> 0
$B^+ Candidate$	Requirement
DIRA	> 0.999
$\chi^2_{End\ Vertex}/N.D.F$	< 25
Vertex Dist. Significance	> 15.0
χ^2_{IP}	< 25
K^+	Requirement
p_T	$> 300 MeV$
p	$> 3000 MeV$
$\chi^2_{Trk}/N.D.F$	< 3.0
χ^2_{IP}	> 9.0
PID_K	> 4
$n_{LongTracks}$	< 250

The L0, Hlt1, and muon ID efficiency varies with respect to the muon kinematics. Thus, we determine the efficiency in bins of muon transverse-momentum and pseudorapidity. The yields used to determine the efficiency are determined by a fit to the invariant mass of the $\mu\mu$ pair. Either sample of *pass* and *fail* events are simultaneously fit with a double-Gaussian signal PDF combined with a first-order Chebychev polynomial function to model the background. The fit is performed for every $p_T - \eta$ kinematic bin, and the total bin-yield of *pass* and *fail* events is extracted from their respective PDF.

A two dimensional correction table is constructed, where each element is the efficiency determined as described above. In the 2017 calibration sample, there are roughtly 1.36M events, with about 428k probe tracks passing the L0, Hlt1, muon identification, and offline selection criteria. The correction table is shown in figure 18. To further illustrate how the efficiency changes with respect to the muon kinematics, projections

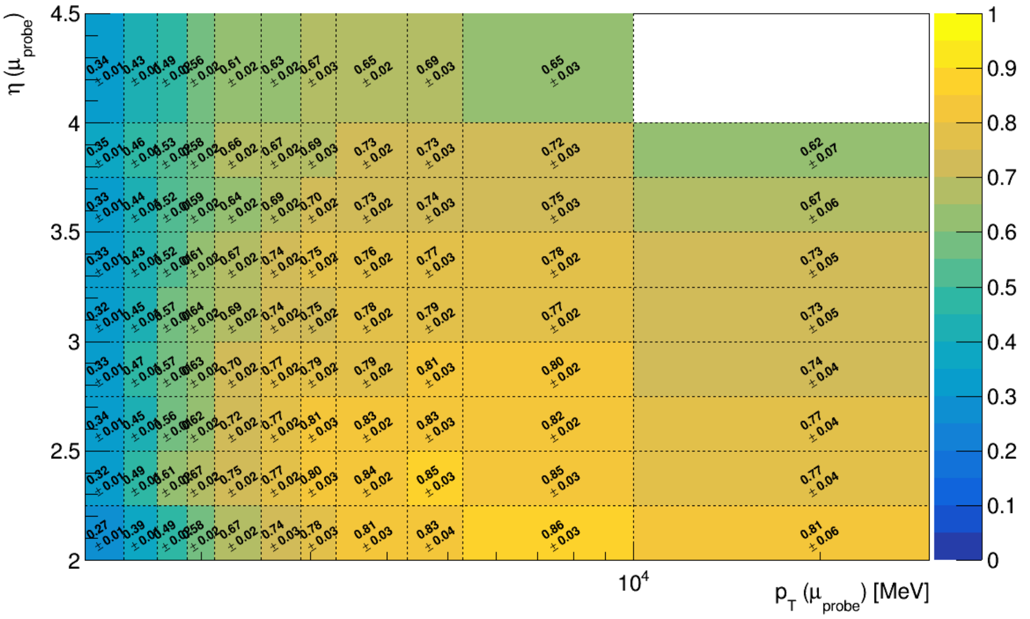

Figure 18: L0, Hlt1, and muon identification efficiency correction table derived from the Tag and Probe method using $B^+ \to (J/\psi\mu^+\mu^-)K^+$ decays, as a function of μ_{probe} pseudorapidity and transverse-momentum.

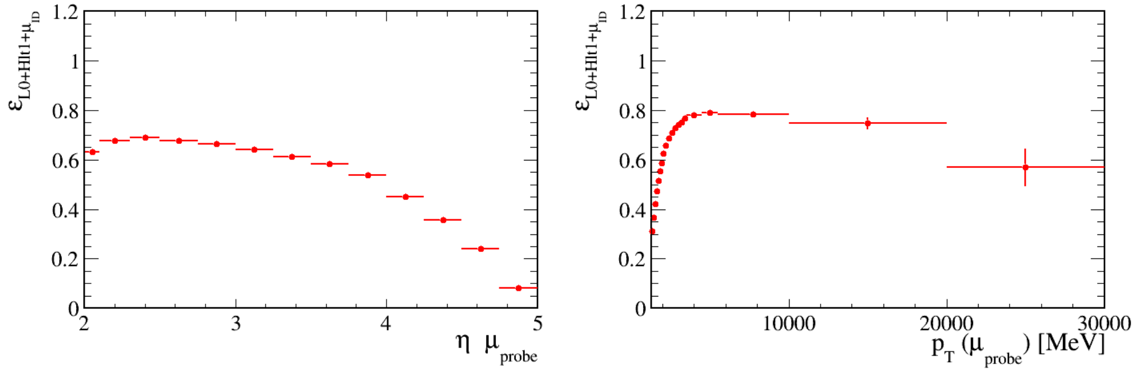

Figure 19: L0, Hlt1, and muon identification efficiencies projected in either μ_{probe} pseudorapidity (left) or μ_{probe} transverse-momentum (right).

of this table are shown either in p_T or η in figure 19.

3.2.2 Hlt2 Efficiency

The efficiency of the Hlt2 trigger is determined by the data-driven TISTOS method [23]. Hlt2 decisions are recorded as either *TIS* or *TOS*, as described in section 3.1.1. To determine the efficiency, the data sample

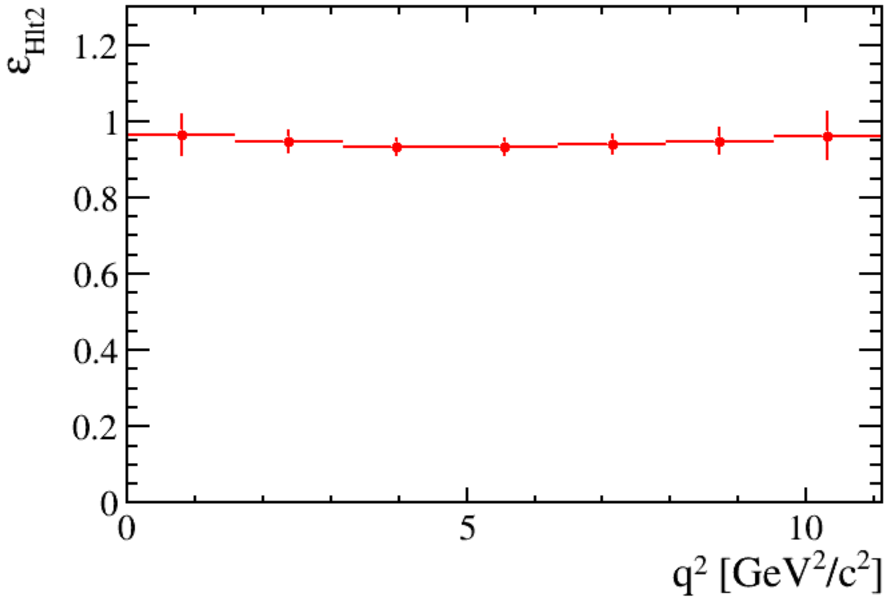

Figure 20: Hlt2 efficiency derived using the $TISTOS$ method as described in the text, as a function of q^2, the invariant mass of the $\mu\overline{\nu}_\mu$ pair.

is processed without any *Hlt2* decision, but all other offline selections are applied. Events are then sorted into two categories: $(TIS\&TOS)$ and $(TIS) \equiv (TIS\&TOS) + (TIS\&!TOS)$. The efficiency is then determined versus q^2:

$$\varepsilon = \frac{N_{(TIS\&TOS)}}{N + (TIS\&TOS) + N_{(TIS\&!TOS)}} \tag{15}$$

To extract the number of events in each category, a simultaneous fit to the $pK^-\pi^+$ invariant mass spectrum is performed for both TIS and $TIS\&TOS$ samples. The signal peak is modeled by a double-Gaussian PDF, and the background shape is modeled by a first-order Chebychev polynomial function. The resulting efficiency is the computed according to equation 15, and shown in figure 20.

3.2.3 Hadron Identification Efficiency

The hadron efficiency of the identification requirements listed in table 5 must also be evaluated using data-driven techniques, as the particle identification (PID) variables in simulation are known to be different than those recorded in data. The PIDCalib package [24] is a software package developed by LHCb designed to estimate the PID efficiencies in the LHCb detector using dedicated calibration samples. The overall efficiency of all PID selections are evaluated separately for protons, kaons, and pions in the data samples.

The calibration samples used by the PIDCalib software use $D^{*+} \to (D^0 \to K^-\pi^+)\pi_s^+$ decays to determine efficiencies of kaon and pion tracks. Proton tracks come from a $\Lambda^0 \to p\pi^-$ sample. Since the kinematics between the calibration samples and the data sample used in this analysis vary, the efficiencies are determined in a three-dimensonal grid of hadron momentum, pseudorapidity, and track multiplicity in the form of the number of hits reconstructed in the SPD detector. All of the other hadron-specific selections from table 5 are applied to the calibration samples. The intervals in which the track efficiencies are computed are reported in table 7. The kinematic dependence of the hadron identification efficiency, projections of this grid are shown in fig. 21 for protons, fig. 22 for kaons, and fig. 23 for pions.

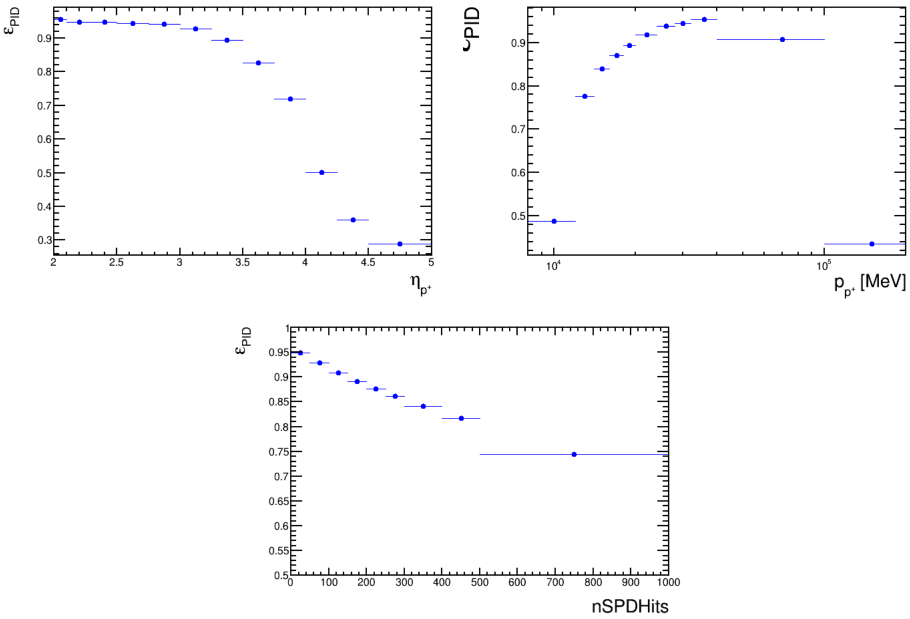

Figure 21: Projections of the hadron identification efficiency, estimated from the PIDCalib2 software package and calibration data samples, for proton tracks with the requirements $(DLLp - DLLK) > 0 \& DLLp > 10$ for proton pseudorapidity(top-left), proton momentum (top-right), and number of hits in the SPD detector (bottom).

Table 7: Kinematic binning used in evaluating hadron PID efficiencies.

Observable	Binning
Proton	
$\overrightarrow{p}(MeV)$	$[8000, 12000, 14000, 16000, 18000, 20000, 24000, 28000, 32000, 40000, 100000, 200000]$
η	$[2, 2.1, 2.3, 2.5, 2.75, 3, 3.25, 3.5, 3.75, 4, 4.25, 4.5, 5]$
$nSPDHits$	$[0, 50, 100, 150, 200, 250, 300, 400, 500, 1000]$
Kaon	
$\overrightarrow{p}(MeV)$	$[2000, 3000, 4000, 7000, 10000, 15000, 20000, 25000, 30000, 40000, 100000]$
η	$[2, 2.1, 2.3, 2.5, 2.75, 3, 3.25, 3.5, 3.75, 4, 4.25, 4.5, 5]$
$nSPDHits$	$[0, 50, 100, 150, 200, 250, 300, 400, 500, 1000]$
Pion	
$\overrightarrow{p}$	$[2000, 3000, 4000, 7000, 10000, 15000, 20000, 25000, 30000, 40000, 100000]$
η	$[2, 2.1, 2.3, 2.5, 2.75, 3, 3.25, 3.5, 3.75, 4, 4.25, 4.5, 5]$
$nSPDHits$	$[0, 50, 100, 150, 200, 250, 300, 400, 500, 1000]$

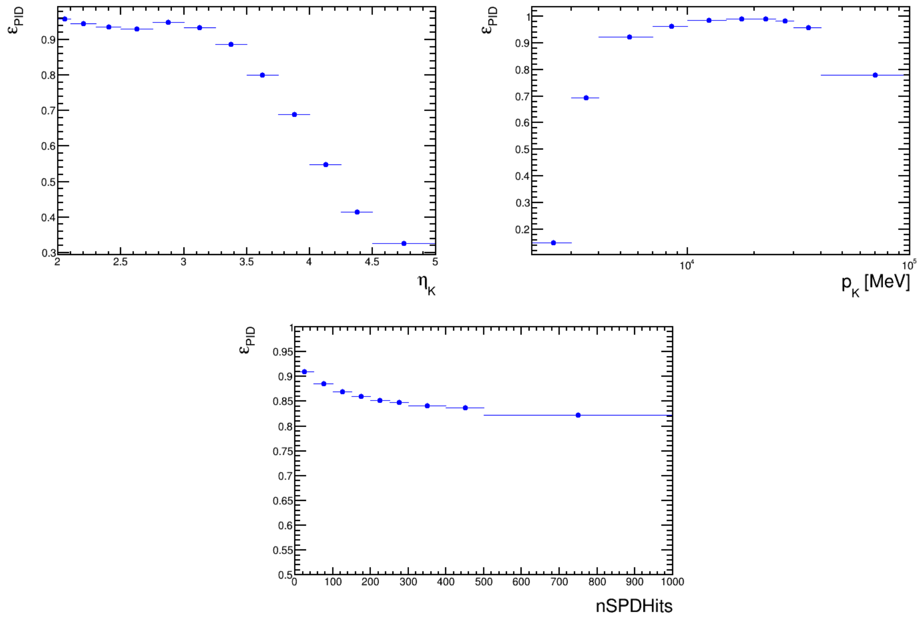

Figure 22: Projections of the hadron identification efficiency, estimated from the PIDCalib2 software package and calibration data samples, for kaon tracks with the requirements $DLLK > 4$ for kaon pseudorapidity (top-left), kaon momentum (top-right), and number of hits in the SPD detector (bottom).

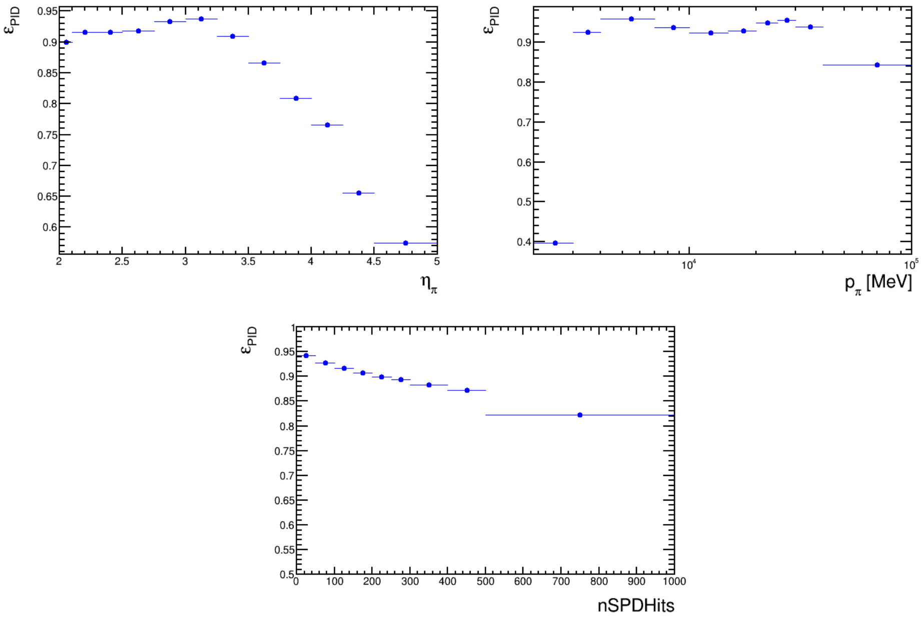

Figure 23: Projections of the hadron identification efficiency, estimated from the PIDCalib2 software package and calibration data samples, for pion tracks with the requirements $DLLp < 0 \& DLLK < 0$ for pion pseudorapidity (top-left), pion momentum (top-right), and number of hits in the SPD detector (bottom).

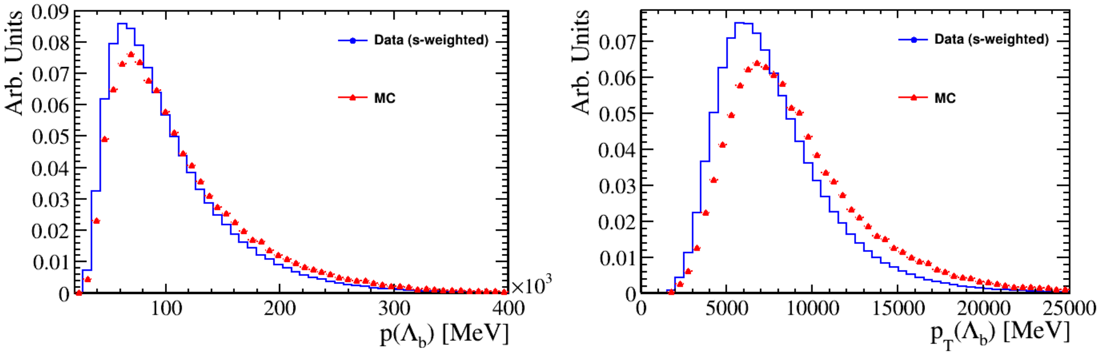

Figure 24: Comparison of Λ_b^0 momentum (left) and transverse-momentum (right) for reconstructed s-Weighted data (blue) and simulated $\Lambda_b^0 \to \Lambda_c^+ \mu^- \overline{\nu}_\mu$ events (red). The p_T distribution is observed to be harder in simulation than in data, which must be corrected for all simulated samples.

3.2.4 Correction of Λ_b^0 Kinematics in Monte Carlo Samples

It is known that Λ_b^0 semileptonic decays are not well modeled in the LHCb detector simulation [20]. This can be seen in fig 24, which shows the $\overrightarrow{p}$ and p_T spectra of the Λ_b^0 in simulation and in data, which has been $s - weighted$ [25] to remove backgrounds. All samples shown have been normalized to unit area. The discrepancy is most apparent in the p_T distribution, in which the data is observed to be much softer than what is produced in simulation.

In order to correct for this effect, a sample of the fully hadronic $\Lambda_b^0 \to J/\psi p K^-$ is reconstructed in real data and in simulation for the 2017 data taking conditions. A fit to the $J/\psi pK$ invariant mass is done for both data and simulation, and a weight is constructed as the ratio of normalized events in simulation to data. Fits are done in intervals of Λ_b^0 $\overrightarrow{p}$ and p_T, detailed in table 8. A 2D correction table is constructed from the computed ratio for each kinematic bin, and is shown in fig 26. Figure 25 shows the Λ_b^0 $\overrightarrow{p}$ and p_T distributions in simulation after the weights have been applied, which are now seen to match more closely to the spectra observed in real data.

Table 8: Momentum and transverse-momentum intervals for correcting simulated Λ_b^0 decays.

Observable	Binning
$\overrightarrow{p}(MeV)$	$[20000, 40000, 60000, 80000, 120000, 160000, 200000, 250000, 300000, 350000, 400000]$
$p_T(MeV)$	$[0, 2000, 4000, 6000, 8000, 12000, 16000, 25000]$

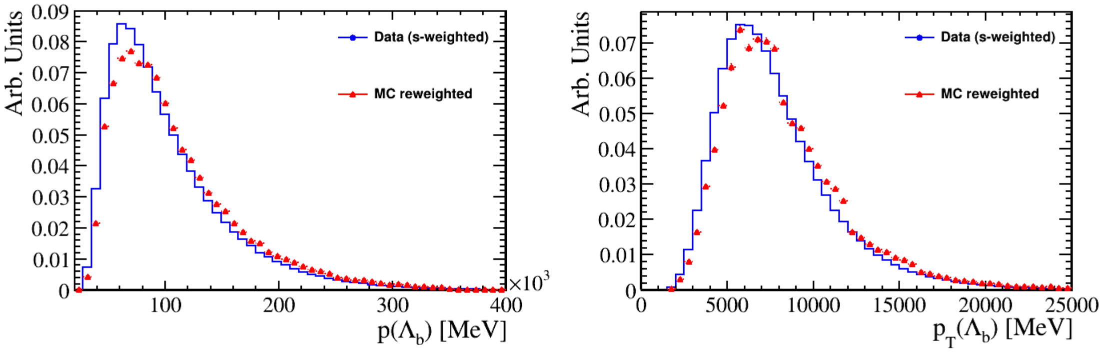

Figure 25: Comparison of Λ_b^0 momentum (left) and transverse-momentum (right) for reconstructed s-Weighted data (blue) and simulated $\Lambda_b^0 \to \Lambda_c^+ \mu^- \overline{\nu}_\mu$ events (red), after weights derived from the hadronic $\Lambda_b^0 \to J/\psi p K^-$ decay channel have been applied.

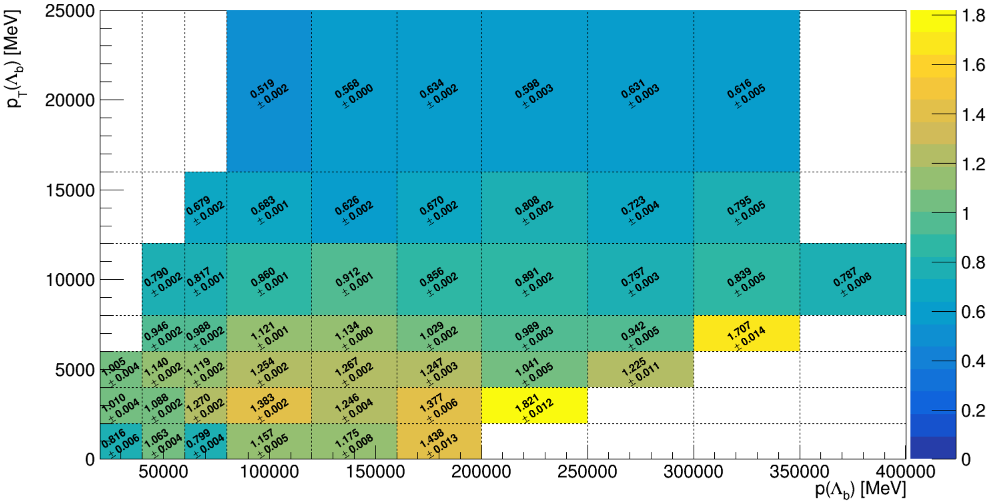

Figure 26: Weight factors derived from the ratio of the number of simulated events to events reconstructed in data using $\Lambda_b^0 \to J/\psi p K^-$ decays. Weights are applied on an event-by-event basis, determined by the Λ_b^0 momentum and Λ_b^0 transverse-momentum of the simulated event.

3.2.5 Total Efficiency Correction Factor

Several Monte Carlo samples have been produced to assess the reconstruction and offline selection efficiency for the final states of interest. These samples are summarized in table 9. Each sample contains both events coming from the Pythia8 event generator with only a cut on the angle of the b flight path to be less than $400 mrad$, as well as events reconstructed through the full LHCb detector description and stripping requirements. The stripping configuration for the latter reconstructed events has been modified to remove any PID or trigger requirements to avoid over correcting for the data derived efficiency estimates.

The simulated events are subject to all other offline selections. Additionally, the charm candidate is ensured to be a signal event by enforcing a requirement on the background category, which utilizes the information of the event's generated particle to reject background modes. The offline and reconstruction efficiency can then be determined as the ratio of the number of reconstructed and selected events, to the total number of generated events in the simulated sample.

The $\varepsilon_{reco.+sel.}$ is weighted according to the data-derived efficiencies on an event-by-event basis, according to the kinematics of the event. The total $\mathit{\Lambda}_b^0$ efficiency is thus determined as:

$$\varepsilon_{total} = \frac{\sum_{evt} n_{evt}^{reco.+sel} \times \varepsilon_{Hlt2} \times [\varepsilon_{L0,Hlt1,\mu_{ID}}(\eta^{\mu_{evt}}, p_T^{\mu_{evt}})] \times [\varepsilon_{had.}(p^{had.}, \eta^{had.}, nSPDhits^{had})]}{N_{genevts.}} \tag{16}$$

The above method is used to correct both the ground state $\mathit{\Lambda}_b^0 \to \mathit{\Lambda}_c^+ \mu \overline{\nu}_\mu$ decay and the $\mathit{\Lambda}_b^0 \to D^0 p \mu \overline{\nu}_\mu$ cross feed channel.

Discrepancies in the tracking system also exist between data and simulation. However, the topologies between the signal mode and normalization channel are such that we reconstruct the same number of tracks with similar kinematic profiles, and thus these effects will cancel in the final determination of the normalized yield $N_{corr}(\mathit{\Lambda}_b^0 \to \mathit{\Lambda}_c^+ \mu^- \overline{\nu}_\mu)$. Following this method, the total efficiency to reconstruct $\mathit{\Lambda}_b^0 \to \mathit{\Lambda}_c^+ \mu^- \overline{\nu}_\mu$ events is 1.152%, and $\mathit{\Lambda}_b^0 \to D^0 p \mu^- \overline{\nu}_\mu$ is 2.08%.

Table 9: List of Monte Carlo samples to study signal and background decay modes. All samples listed are generated using according to the 2017 data taking conditions of the LHCb detector, and processed with Stripping version 29r2, with PID and Trigger requirements removed.

Decay Mode	Nickname	# Generated Events
$\mathit{\Lambda}_b^0 \to \mathit{\Lambda}_c^+ \mu^- \overline{\nu}_\mu$	$Lb\_Lcmunu, pKpi = cocktail, Baryonlnu$	$17M$
$\mathit{\Lambda}_b^0 \to D^0 p \mu^- \overline{\nu}_\mu$	$Lb\_D0pmunu, D0\_Kpi = LHCbAcceptance$	$3M$
$\mathit{\Lambda}_b^0 \to \Lambda_c(2595)^+ \mu^- \overline{\nu}_\mu$	$Lb\_Lc2593munu, Lcpipi, pKpi = LHCbAcceptance$	$3M$
$\mathit{\Lambda}_b^0 \to \Lambda_c(2625)^+ \mu^- \overline{\nu}_\mu$	$Lb\_Lc2625munu, Lcpipi, pKpi = LHCbAcceptance$	$3M$
$\mathit{\Lambda}_b^0 \to \Lambda_c(2765)^+ \mu^- \overline{\nu}_\mu$	$Lb\_Lc2765munu, Lcpipi, pKpi = LHCbAcceptance$	$3M$
$\mathit{\Lambda}_b^0 \to \Lambda_c(2880)^+ \mu^- \overline{\nu}_\mu$	$Lb\_Lc2880munu, Lcpipi, pKpi = LHCbAcceptance$	$3M$
$\mathit{\Lambda}_b^0 \to \mathit{\Lambda}_c^+ (D_s \to \mu^- \overline{\nu}_\mu X)$	$Lb\_LcDs, pKpi, Xmunu, cocktail = LHCbAcceptance$	$4M$

3.3 Neutrino Reconstruction

Due to the presence of a neutrino in the final state, the decay $\Lambda_b \to \Lambda_c \mu \overline{\nu}_\mu X$ can never be fully reconstructed. This section will describe the method used to reconstruct the Λ_b momentum, accounting for the missing momentum carried by the neutrino.

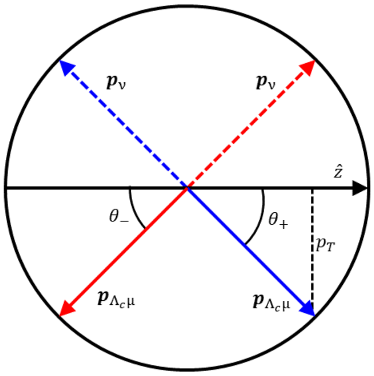

Figure 27: The decay $\Lambda_b^0 \to \Lambda_c^+ \mu^- \overline{\nu}_\mu$ in the Λ_b^0 rest frame. Since the $\overline{\nu}_\mu$ cannot be reconstructed, its orientation with respect to the Λ_b^0 fight direction ($\hat{z}$), is unknown, leading to two scenarios: the θ_- case, in which $p_{\overline{\nu}_\mu}^{\|}$ is oriented opposite to $\overrightarrow{p}_{\Lambda_b^0}$, and the θ_+ case, where $p_{\overline{\nu}_\mu}^{\|}$ and $\overrightarrow{p}_{\Lambda_b^0}$ are aligned.

3.3.1 Kinematic Framework

To solve for the missing Λ_b momentum, it is convenient to work in the rest frame of the Λ_b, as the decay kinematics can be fully determined if we assume that the invariant mass of the $\Lambda_c^+\mu$ system is:

$$E_{\Lambda_c\mu}^{CM} = \frac{m_{\Lambda_b^0}^2 + m_{\Lambda_c}^2}{2m_{\Lambda_b^0}} \tag{17}$$

and thus total momentum of the $\Lambda_c\mu$ system may be computed as:

$$p_{\overline{\nu}_\mu}^{CM} \equiv p^{CM} = \frac{m_{\Lambda_b}^2 - m_{\Lambda_c\mu}^2}{2m_{\Lambda_b}} \tag{18}$$

The transverse component of this vector is defined as the perpendicular component with respect to the Λ_b flight direction, as shown in figure 27, which can be computed directly. In the Λ_b rest frame, the neutrino momentum vector has an equal magnitude and opposite direction to that of the $\Lambda_c\mu$ system. Next, we define θ as the angle between the $\Lambda_c\mu$ momentum vector and the Λ_b flight path, and is simply computed as:

$$sin\theta = \frac{p_T^{\Lambda_c\mu}}{p^{CM}} \tag{19}$$

Some reconstructed events may be nonphysical, which appear when the ratio $p_T^{\Lambda_c\mu}/p^{CM} > 1$. For these events, we discard those in which the ratio is > 1.1. For events where $1 < p_T^{\Lambda_c\mu}/p_{\Lambda_c\mu}^{CM} < 1.1$, the ratio is set equal to 1.

Unfortunately, the orientation of the neutrino with respect to the Λ_b flight path is unknown. Therefore, we can only solve for the missing momentum up to a two-fold ambiguity. The boost from the $\mathit{\Lambda}_b^0$ rest frame to the laboratory frame is defined by the relationships:

$$\sqrt{1-\beta^2 p_{\parallel,lab}^2} = \beta E^{CM} + p^{CM} \times \cos\theta \tag{20}$$

and

$$p_T^{\Lambda_c\mu} = |p^{CM} \sin\theta| \tag{21}$$

Squaring equation 20 yields a quadratic equation for β:

$$(\beta^2-1)p_{\parallel,lab}^2 + 2p_{\Lambda_c\mu}^{CM}\cos\theta E_{\Lambda_c\mu}\beta + p_{\Lambda_c\mu}^{CM}\cos\theta^2 \tag{22}$$

Solving equation 22 yields the two solutions

$$\beta_\pm = \frac{-E_{\Lambda_c\mu}^{CM} p^{CM} cos\theta_\mp \pm \sqrt{p_{\Lambda_c\mu}^2 E_{\Lambda_c\mu}^{2CM} cos^2\theta_\mp + (E_{\Lambda_c\mu}^{2Lab} - E_{\Lambda_c\mu}^{2CM})(E_{\Lambda_c\mu}^{2Lab} + p_{\Lambda_c\mu}^2 cos^2\theta_\mp)}}{E_{\Lambda_c\mu}^{2Lab} + p_{\Lambda_c\mu}^2 cos^2\theta_\mp} \tag{23}$$

The solutions $\beta_\pm$ allow the Λ_b momentum to be computed:

$$p_\pm^{\Lambda_b} = \frac{m_{\Lambda_b}\beta_\pm}{\sqrt{1-\beta_\pm^2}} \tag{24}$$

Since the p_{Λ_b} can only be known up to a two-fold ambiguity, one solution must be chosen. In equation 23, the angle θ_+ indicates that the parallel component of the $\Lambda_c\mu$ momentum vector is aligned with the Λ_b flight direction, and the neutrino is pointing in the opposite direction, corresponding to the solution with the lower boost, β_-. In the second case, the neutrino is pointing forward, which corresponds to the higher boost scenario, or the β_+ solution. This is illustrated in blue for β_- and red for β_+ in figure 27. Figure 28 shows the distribution of $\cos\theta$ in simulated $\mathit{\Lambda}_b^0 \to \mathit{\Lambda}_c^+\mu\overline{\nu}_\mu$ events, where it can be seen that there is a slight preference for events corresponding to the β_- solution, and thus this is the choice made for this analysis.

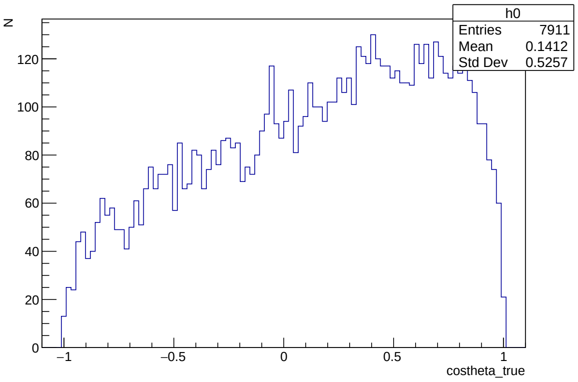

Figure 28: Spectrum of $\cos\theta_{\mathrm{CM}}$ for a sample of $\Lambda_b^0 \to \Lambda_c^+ \mu^- \overline{\nu}_\mu$ generated events.

Finally, the calculated p_{Λ_b} is used to determine q^2:

$$q^2 = (p_{\Lambda_b} - p_{\Lambda_c})^2 \tag{25}$$

3.4 The Corrected Yield $N_{corr}(\Lambda_b^0 \to \Lambda_c^+ \mu^- \overline{\nu}_\mu)$

To determine $|V_{cb}|$, the total yield of $\Lambda_b^0 \to \Lambda_c^+ \mu^- \overline{\nu}_\mu$ events must be compared with the total width $\Gamma(\Lambda_b^0 \to \Lambda_c^+ \mu^- \overline{\nu}_\mu)$ predicted from the lattice calculations of Ref. [9]. The total raw yield must first be determined over the full q^2 range, from 0 to the maximum value 11.098 GeV^2/c^2, when the Λ_c^+ baryon is produced at rest in the Λ_b^0 center-of-mass frame. A chi-square fit to the Λ_b^0 corrected mass spectrum is performed, which includes templates derived from simulation. The components included in the fit are summarized in table 10. In addition to the signal channel, the templates account for contributions coming from the higher mass $\Lambda_b^0 \to \Lambda_c^{+*} \mu^- \overline{\nu}_\mu$ decays, as well as backgrounds coming from a Λ_b^0 decaying into a Λ_c^+ plus another charmed hadron that decays semileptonically. The specific decay modeled in the fit is $\Lambda_b^0 \to \Lambda_c^+ (D_s \to \mu^- \overline{\nu}_\mu) X$. The template shapes, normalized to unit area, are shown in fig 29. The template shape for the background coming from random combinations of tracks with a Λ_c^+ baryon is inferred from wrong-sign (WS) events reconstructed in data, where the μ and Λ_c^+ have the same sign charge.

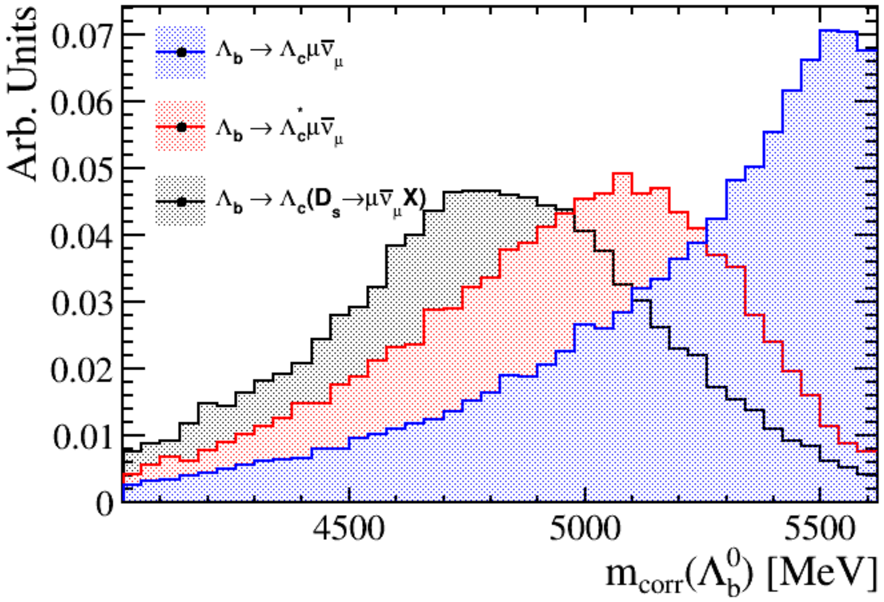

Figure 29: Corrected mass template shapes from simulated events. The $\Lambda_b^0 \rightarrow \Lambda_c^+ \mu^- \overline{\nu}_\mu$ signal is shown by the blue histogram, and the various background modes included in the corrected mass fit are listed in the legend.

Table 10: Template shapes derived from Monte Carlo simulation used by the chi-square fit to the Λ_b^0 corrected mass.

Component	Purpose (Source)
$\Lambda_b^0 \rightarrow \Lambda_c^+ \mu^- \overline{\nu}_\mu$	$Signal\ Shape(MC)$
$\Lambda_b^0 \rightarrow \Lambda_c^{+*} \mu^- \overline{\nu}_\mu$	$Excited\ \Lambda_c^+\ Background(MC)$
$\Lambda_b^0 \rightarrow \Lambda_c^+ (D_s \rightarrow \mu^- \overline{\nu}_\mu X)$	$Double - Charm\ Background(MC)$
$\Lambda_b^0 \rightarrow \Lambda_c^+ \mu^+ \overline{\nu}_\mu$	$Combinatoric\ Background(WS\ Data)$

The Λ_b^0 corrected mass is distributed in 40 bins over the range [4020:5620], with a uniform 40MeV bin size. The fit yields 1.45M signal events, with a fit-$\chi^2/N.D.F$ vaule of 1.38. The precise results from the fit are summarized in table 11.

Table 11: Measured event yields of signal and background modes from the chi-square fit to the Λ_b^0 corrected mass distribution of the 2017 data set.

Fit Component	Yield
$\Lambda_b^0 \rightarrow \Lambda_c^+ \mu^- \overline{\nu}_\mu (signal)$	1518940 ± 10529.0
$\Lambda_b^0 \rightarrow \Lambda_c^{+*} \mu^- \overline{\nu}_\mu (background)$	696755 ± 1268.9
$Lb \rightarrow \Lambda_c^+ (D_s^{(*)} \rightarrow \mu \overline{\nu}_\mu X)(double - charm\ background)$	4643.68 ± 2304.9
$Combinatoric\ Background$	97659.7 ± 9181.08

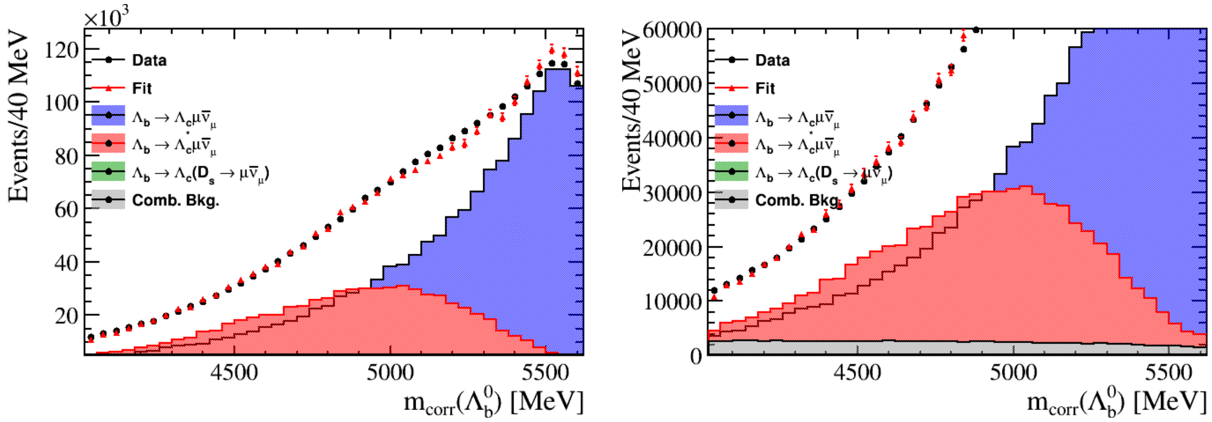

Figure 30: Fit to the corrected mass in the 2017 data set. The data is displayed as black points, while the fit result is shown as the red points. The various fit components are listed in the legend. Some components are imperceptible in the nominal plot (left), therefore the right hand plot with a limited range of the y-axis is included to show the additional included templates (right).

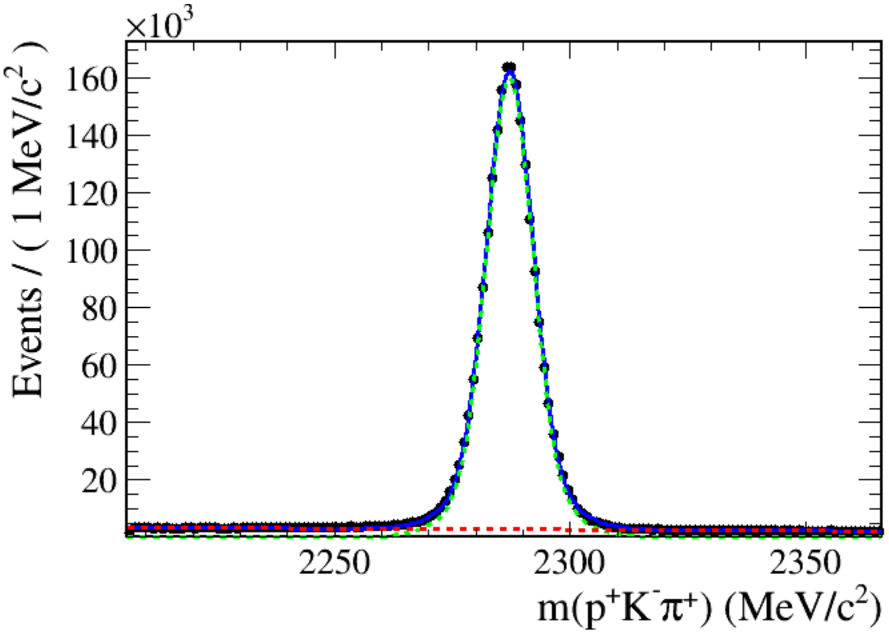

Figure 31: Fit to the invariant $pK^-\pi^+$ mass used to determine the total $N_{Raw}(\Lambda_b^0 \to \Lambda_c^+\mu^-\overline{\nu}_\mu X)$ yield for the 2017 data set. The signal shape is shown by the dashed green curve, and the background by the dashed red curve. The blue curve shows the total PDF.

3.5 Normalization to the Inclusive $\Lambda_b^0 \to X_c\mu^-\overline{\nu}_\mu$ Mode

The total corrected yield is normalized to the total event yield from the inclusive $\Lambda_b \to X_c\mu^-\overline{\nu}_\mu X$ decay mode. Equation 11 is broken up into two terms, where the first term covers Λ_b^0 baryons decaying to a Λ_c^+ baryon plus a $\mu^-\overline{\nu}_\mu$ pair, including contributions from the higher mass Λ_c^{+*} decays. The second term arises from $\Lambda_b^0 \to D^0p\mu^-\overline{\nu}_\mu$ decays, with the additional factor κ to account for D^+n final states.

3.5.1 The final state $\Lambda_b^0 \to \Lambda_c^+\mu^-\overline{\nu}_\mu X$

The raw yield of $\Lambda_b^0 \to \Lambda_c^+\mu^-\overline{\nu}_\mu X$ events, the numerator of the first term in equation 11, is determined via a binned maximum likelihood fit to the mass spectrum of the Λ_c decay products, $p^+K^-\pi^+$, in 160 bins over the range $|m(\Lambda_c^+)_{pdg}| < 80MeV$. The shape is described by a PDF consisting of a double-Gaussian to model the signal, combined with a Chebychev polynomial representing the background contribution. The background shape is controlled by fitting to the right-sign sample, in which the Λ_c baryon and μ have opposite charge, and simultaneously fitting to wrong-sign events, where the Λ_c and μ have like charges. The resulting fit can be seen in figure 31, which yields 2.14M signal events and 430k background events. The precise results from the right-sign sample are summarized in table 12.

Table 12: Measured yields for $\Lambda_b^0 \to \Lambda_c^+ \mu^- \overline{\nu}_\mu X$ decays in the 2017 data set.

Component	Yield
Signal ($\Lambda_c^+ \mu^- \overline{\nu}_\mu$)	2138359.97 ± 1595.06
Background (RS sample)	429607.45 ± 884.15

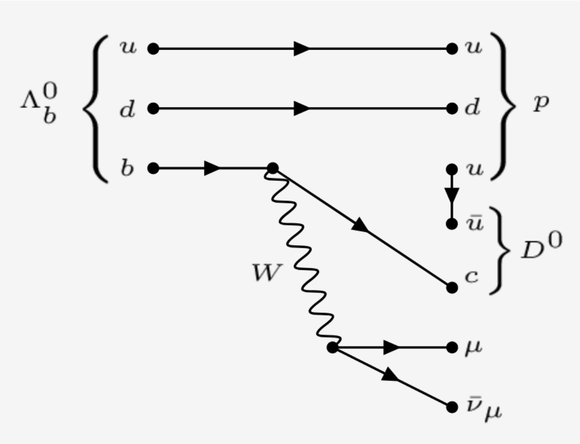

Figure 32: Feynman diagram for the decay $\Lambda_b^0 \to D^0 p \mu^- \overline{\nu}_\mu$.

3.6 The final state $\Lambda_b^0 \to D^0 p \mu^- \overline{\nu}_\mu$

Λ_b^0 baryons can also decay into $\Lambda_b^0 \to D^0 p \mu^- \overline{\nu}_\mu$ final states, as shown in the Feynman diagram in fig 32. To extract the yields, we first reconstruct the $\Lambda_b^0 \to D^0 p \mu^- \overline{\nu}_\mu$ events by applying the selections from table 5 to events output from the *StrippingB2DMuNuX_D0* line. Backgrounds are subtracted by constructing s-weights via a simultaneous fit to the D^0 mass spectrum on both right-sign and wrong-sign events, where the wrong sign is defined as and event in which a D^0 is combined with an anti-proton.

As seen in [20], there is a large signal component coming from non-resonant Λ_b^0 decays. Therefore, 1-dimensional fit to the mass is insufficient to model the broad non-resonant spectrum, which overlaps with the combinatoric background. To help isolate signal $\Lambda_b^0 \to D^0 p \mu^- \overline{\nu}_\mu$ events, a second fit variable is introduced. The observable $ln(\Delta\chi^2_{vtx.})$ is utilized, which is defined as the logarithm of the difference in the χ^2 value of the vertex fit of the $D\mu$ system, and the χ^2 of the secondary vertex fit when the additional proton candidate. Both resonant and non-resonant signal decays will peak in this spectrum, while the background follows a smooth exponential rise, making this a valuable tool in discriminating signal from background.

Three resonant peaks are observed in the mass spectrum, corresponding to $\Lambda_c^+(2860)$, $\Lambda_c^+(2880)$, and $\Lambda_c^+(2940)$, which have also been observed in [26] and [27]. An overview of the fit components and the PDF shapes used to model each is summarized in table 13. To model the $\Lambda_c^+(2860)$ resonance near the $D^0 p$

threshold mass, a signal PDF is constructed from the sum of two Bifurcated Gaussian shapes with a shared mean, convoluted with a Gaussian. The parameters describing the shape are fixed using an iterative procedure to their best-fit values. The narrower $\Lambda_c^+(2880)$ is described by a relativistic Breit-Wigner (RBW) function convoluted with a Gaussian. The RBW has the form

$$RBw(m) = \frac{\Gamma(m)}{(m^2 - m_R^2) + (m_R \Gamma(m))^2} \tag{26}$$

where m is the observed D^0p mass, m_R is the mass of the resonant from the PDG, and $\Gamma(m)$ is the mass-dependent width:

$$\Gamma(m) = \Gamma_0 \frac{m_R}{m} \frac{k}{k_R} (\frac{q}{q_R})^{(2s+1)} \tag{27}$$

$$q(m, m_R) = \frac{1}{2m} \sqrt{[m^2 - (m_{D^0} + m_p)^2][m^2 - (m_{D^0} - m_p)^2]} \tag{28}$$

$$k(m, m_R) = \frac{1}{z^4 + 3z^2 + 9}, z = q\rho \tag{29}$$

Here, Γ_0 and ρ are fit parameters, and $s = 2$, corresponding to the spin of the $\Lambda_c^+(2880)$ baryon, which is assumed to have total angular momentum $j = 5/2$. . The third $\Lambda_c^+(2940)$ is observed to be very broad, and a simple Gaussian is used to model the peak. The background and non-resonant components are described by a threshold function:

$$f(m) = (m - m_0)^{\alpha} e^{-\beta m} \tag{30}$$

where m is the observed invariant mass, m_0 is the threshold D^0p mass and α and β are fit parameters.

A two dimensional binned maximum likelihood fit to the D^0p mass and $ln(\Delta\chi^2_{vtx.})$ is performed. To help control the background and non-resonant shapes, and to better resolve the resonant peaks, the fit is broken up into two mass regions, ranging from the threshold D^0p mass around $2805 MeV$ to $3000 MeV$, and $3000 MeV$ to $5000 MeV$, where the higher mass window contains only contributions from non-resonant and combinatoric background components. Simultaneous fits to both the right-sign and wrong-sign events are performed for both the lower mass window (figure 33), and for the higher mass window (figure 34). The resulting yield of signal events is the combined total of resonant and non-resonant events extracted from the fit: 70513 ± 627 events. See table 14 for the complete summary of the yields extracted from each fit component.

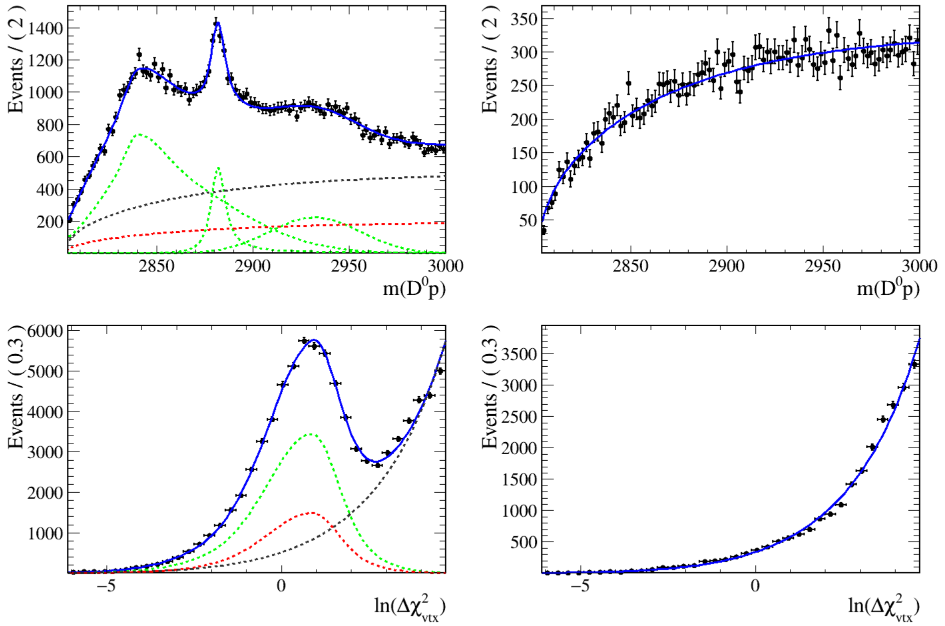

Figure 33: Two dimensional fit results to the spectra $m(D^0p)$ (*top*) and $ln(\Delta\chi^2_{vtx.})$ (*bottom*) to determine the yield of $\Lambda_b^0 \to D^0 p\mu^-\overline{\nu}_\mu$ decays in the 2017 data over the range $m(D^0p)[2805:3000]MeV$. The right-sign sample (*left*) is fit simultaneously with the wrong-sign sample (*right*). The resonant signal component is represented by dashed green lines, while the non-resonant signal component appears as dashed red lines. The combinatoric background appears as the dashed gray curve, and the total fit PDF is the solid blue line.

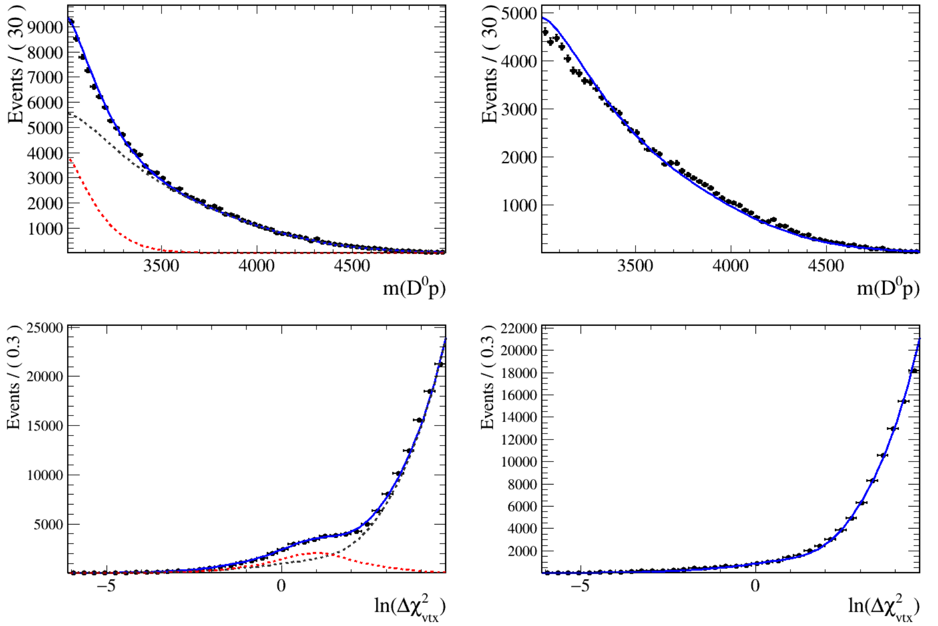

Figure 34: Two dimensional fit results to the spectra $m(D^0p)$(*top*) and $ln(\Delta\chi^2_{vertex})$ (*bottom*) to determine the yield of $\Lambda_b^0 \to D^0 p\mu^-\overline{\nu}_\mu$ decays in the 2017 data over the range $m(D^0p)[3000:5000]MeV$. The right-sign sample (*left*) is fit simultaneously with the wrong-sign sample (*right*). There is no discernible resonant signal in this mass region. The non-resonant signal component appears as dashed red lines. The combinatoric background appears as the dashed gray curve, and the total fit PDF is the solid blue line.

Table 13: Components and PDF shapes used in the fit to the $\mathit{\Lambda}_b^0 \to D^0 p\mu^-\overline{\nu}_\mu$ mass and $ln(\Delta\chi^2_{Vtx})$ spectra as described in the text.

Component	$m(D^0p)[2805:3000]MeV$	$ln(\Delta\chi^2_{vertex})$
$\Lambda_c(2860)^+$	$double-bifurcated\ Gaussian \otimes Gaussian$	$double-bifurcated\ Gaussian$ $(resonant+non-resonant)$
$\Lambda_c(2880)^+$	$relativisticBreit-Wigner \otimes Gaussian$	
$\Lambda_c(2940)^+$	$double-Gaussian$	
$Non-resonant$	$Thresholdfunction+Gaussian$	
$Combinatoric\ Background$	$thresholdfunction+Gaussian$	$exponential+Gaussian$
Component	$m(D^0p)[3000:5000]MeV$	$ln(\Delta\chi^2_{vertex})$
$Non-resonant$	$threshold\ function+Gaussian$	$double-bifurcatedGaussian$
$Combinatoric\ Background$	$threshold\ function+Gaussian$	$exponential+Gaussian$

Table 14: Extracted $\mathit{\Lambda}_b^0 \to D^0 p\mu^-\overline{\nu}_\mu$ yields from the two dimensional fit to the $m(D^0p)$ and $ln(\Delta\chi^2_{vtx.})$

Component	Yield
$\Lambda_c(2860)^+$	23296.40 ± 249.33
$\Lambda_c(2880)^+$	3670.86 ± 132.57
$\Lambda_c(2940)^+$	6544.07 ± 236.31
$Non-resonant$	36912.10 ± 507.57
$Combinatoric\ Background$	148551.65 ± 493.13

4 Results

Lattice calculations presented by Ref. [9] provide a theoretical estimate of $\Gamma_{Th.}(\Lambda_b^0 \to \Lambda_c^+ \mu^- \overline{\nu}_\mu)/|V_{cb}|^2$. A measurement of $|V_{cb}|$ can therefore be obtained by comparing the measured semileptonic width $\Gamma_{Meas.}(\Lambda_b^0 \to \Lambda_c^+ \mu^- \overline{\nu}_\mu)$ with the theoretical prediction, where $|V_{cb}|^2$ is the normalization factor between the measured and predicted widths. The measured width is obtained using the method detailed in the previous chapter. The measured raw yield $N_{raw}(\Lambda_b^0 \to \Lambda_c^+ \mu^- \overline{\nu}_\mu)$ extracted from the fit to the Λ_b^0 corrected mass is:

$$N_{raw} = 1449420 \pm 13166.7 \text{ events}$$

The raw yield is then corrected for detector efficiencies and for the charm branching fraction $\mathcal{B}(\Lambda_c^+ \to pK^-\pi^+)$. The total efficiency correction, determined from both data-driven techniques and from simulation, is $\varepsilon_{total} = (1.152 \pm 0.028\%)$ Charm branching fractions for the decay $\Lambda_c^+ \to pK^-\pi^+$ have been measured by [28] and [29]. A weighted average of these measurements is used to correct the raw yield for this analysis. Furthermore, the branching fraction $\mathcal{B}(D^0 \to K^-\pi^+)$ is recorded in the PDG [4]. The measurements and uncertainties of the branching fractions used in this analysis are documented in table 15.

Table 15: Charm branching fractions used to correct the measured yields $N_{raw}(\Lambda_b^0 \to \Lambda_c^+ \mu^- \overline{\nu}_\mu)$ and $N_{raw}(\Lambda_b^0 \to D^0 p \mu^- \overline{\nu}_\mu)$ for both signal and normalization channels.

Particle & Decay	$\mathcal{B}(\%)$	Relative error (%)	Source
$\Lambda_c^+ \to pK^-\pi^+$	6.23 ± 0.33	4.0	Weighted average of [28] and [29]
$D^0 \to K^-\pi^+$	3.93 ± 0.05	1.3	PDG average [4]

Applying the correction factors to the raw yield provides the total corrected yield $N_{corr}(\Lambda_b^0 \to \Lambda_c^+ \mu^- \overline{\nu}_\mu) = (2.02 \pm 0.109) \times 10^9$ events.

4.1 Normalization to $n_{corr}(\Lambda_b^0 \to X_c \mu^- \overline{\nu}_\mu)$

The total corrected yield must be normalized by the total yield of reconstructed $\Lambda_b^0 \to X_c \mu^- \overline{\nu}_\mu X$ events in order to determine the semilptonic width $\Gamma(\Lambda_b^0 \to \Lambda_c^+ \mu^- \overline{\nu}_\mu)$. The yield of $\Lambda_b^0 \to \Lambda_c^+ \mu^- \overline{\nu}_\mu X$ decays is extracted from the one-dimensional fit to the $m(pK^-\pi^+)$ mass spectrum. The measured value listed in table 12 is 2138359.97 ± 1595.06 events. The total yield of resonant and non-resonant signals for the cross feed channel $\Lambda_b^0 \to D^0 p \mu^- \overline{\nu}_\mu$ is extracted from the two dimensional fit to the $m(D^0 p)$ and $ln(\Delta\chi^2_{vtx.})$ spectra and listed in table 14 is 70513.43 ± 627.06 events. After correcting for the measured efficiency and charm branching fractions for either channel, the total corrected yield is evaluated following equation 11, is $n_{corr} = (3.10 \pm 0.174) \times 10^9$ events.

4.2 Measurement of the Branching Fraction $\mathcal{B}(\Lambda_b^0 \to \Lambda_c^+ \mu^- \overline{\nu}_\mu)$

The procedure of determining $|V_{cb}|$ also provides a method to measure the exclusive branching fraction $\mathcal{B}(\Lambda_b^0 \to \Lambda_c^+ \mu^- \overline{\nu}_\mu)$. Using the measured yields $N_{corr}(\Lambda_b^0 \to \Lambda_c^+ \mu^- \overline{\nu}_\mu)$ and $N_{corr}(\Lambda_b^0 \to X_c \mu \overline{\nu}_\mu)$, we can evaluate the exclusive branching fraction as

$$\mathcal{B}(\Lambda_b^0 \to \Lambda_c^+ \mu^- \overline{\nu}_\mu) = \frac{n_{corr}(\Lambda_c^+ \mu)}{n_{corr}(X_c \mu)} \cdot \frac{\mathcal{B}_{SL}(\langle B^{0,+} \rangle)}{\tau_{\langle B \rangle}} \cdot \tau_{\Lambda_b^0} \cdot (1 - \xi) \tag{31}$$

where once again the shorthand $X\mu$ is used to represent the decay $\Lambda_b^0 \to X \mu^- \overline{\nu}_\mu$. The remaining inputs include the measured lifetimes and branching fractions listed in table 3, where once again the factor ξ is a small (3%) correction. The measured branching fraction is

$$\mathcal{B}(\Lambda_b^0 \to \Lambda_c^+ \mu^- \overline{\nu}_\mu) = (6.30 \pm 0.39)\%.$$

4.2.1 Measurement of the CKM Parameter $|V_{cb}|$

The exclusive semileptonic width $\Gamma(\Lambda_b^0 \to \Lambda_c^+ \mu^- \overline{\nu}_\mu)$ can be obtained from equation 13. The corrected yields for the ground state $\Lambda_b^0 \to \Lambda_c^+ \mu^- \overline{\nu}_\mu$ and the inclusive $\Lambda_b^0 \to X_c \mu^- \overline{\nu}_\mu$ have been measured and reported previously in this study. The inclusive width $\Gamma(\Lambda_b^0 \to X_c \mu^- \overline{\nu}_\mu)$ is determined from equation 10 using the inputs from s [4] [5], listed in table 3. From the measurements in this study is determined:

$$\Gamma_{Meas}(\Lambda_b^0 \to \Lambda_c^+ \mu^- \overline{\nu}_\mu) = (4.103 \pm 0.106) \times 10^{-2} \text{ps}^{-1}$$

Comparing this to the total predicted width from Ref. [9]

$$\Gamma_{Th.}(\Lambda_b^0 \to \Lambda_c^+ \mu^- \overline{\nu}_\mu)/|V_{cb}|^2 = (21.1 \pm 0.8) \text{ps}^{-1}$$

allows a preliminary determination of $|V_{cb}|$ to be computed directly:

$$|V_{cb}| = (44.1 \pm 1.01) \times 10^{-3}$$

4.3 Uncertainties and Ongoing Studies

The full study of statistical and systematic uncertainties for this analysis is ongoing. We expect several sources to contribute to the overall uncertainties for both the branching fraction $\mathcal{B}(\Lambda_b^0 \to \Lambda_c^+ \mu^- \overline{\nu}_\mu)$ measurement and the measured $|V_{cb}|$ value, which are listed in table 16. However, due to the topologies in the signal and normalization channels, we expect many of these uncertainties to cancel in the final evaluations.

Source
MC Statistics
MC Modeling
Trigger Efficiency (L0, Hlt1, Hlt2)
PID Efficiency
Λ_b^0 MC re-weighting corrections
Choice of q^2 solution
Templates for $m_{corr}(\Lambda_b^0)$ Fit
PDF shapes for normalization channels

Table 16: Expected sources of systematic uncertainties to be assessed for the measurements reported in this study.

4.3.1 Data Driven Efficiencies

The data driven efficiencies considered arise from the Trigger, muon ID, and hadron identification. We first consider the L0, Hlt1, and Muon ID efficiency, which is derived from the calibration sample of detached $J/\psi \to \mu\mu$ events. As was shown in the preceding chapters, this efficiency is highly dependent on the muon kinematics. The choice of μ_{probe} binning and statistical uncertainties of the sample will be studied using toy simulations, where the quoted uncertainties will be allowed to vary within their errors according to a Gaussian distribution. However, due to the similarities of the muon kinematics in both the signal $\Lambda_b^0 \to \Lambda_c^+ \mu^- \overline{\nu}_\mu$ and the normalization $\Lambda_b^0 \to X_c \mu^- \overline{\nu}_\mu$ channels, these effects are expected to completely cancel.

The uncertainty on the Hlt2 trigger arises from the limited statistics of the TIS sample in each q^2 bin. Once again, these effects should largely cancel due to the similarities in the final states studied.

The uncertainties in the hadron identification can arise from several sources, including the statistical uncertainty attributed to the calibration samples used, as well as the kinematic binning used for each track. To assess the level of the uncertainties, two approaches are planned. First, toy simulations will be used to estimate the statistical uncertainty, where the quoted efficiencies will be allowed to vary within their errors, for each kinematic bin, according to a Gaussian distribution. The overall PID efficiency will then be re-calculated using the same manner, and the differences assessed. To study the systematic uncertainty associated with the kinematic binning, alternate binning schema will be used and PID efficiencies will be determined for identification variables coming from simulation. The evaluation the PID selection efficiency will then be compared to the data-driven values to assess the uncertainty.

4.3.2 Kinematic Re-weighting Uncertainty

Monte Carlo samples in this analysis were corrected for Data/MC discrepancies in the Λ_b^0 kinematics. This was done using the hadronic $\Lambda_b^0 \to J/\psi p K$ decay, where the weight factor was determined by fits to the

$J\psi$ mass peak in both MC and data, and constructing the ratio between the resulting normalized yields. To assess the systematic uncertainty on this technique, alternate binnings in $\overrightarrow{p}(\Lambda_b^0)$ and $p_T(\Lambda_b^0)$ will be studied.

4.3.3 Choice of q^2 solution

When reconstructing the neutrino in order to determine the Λ_b^0 momentum, the solution corresponding to the lower boost was chosen based on the preference of the $p_{\parallel}^{CM}(\nu)$ to be pointed anti-parallel to the Λ_b^0 flight direction as observed in generator-level simulated events. This may, however, not always match the kinematics of the true decay in data.

An alternative method of choosing the *best* solution is being studied. This method employs a linear regression algorithm based on the SCIKIT Learn package [30], which uses two well-measured properties of the reconstructed Λ_b^0: the sine of the angle of the flight direction with respect to the proton beam direction, and the flight distance. The algorithm uses this information to infer the Λ_b^0 momentum. Then, the choice of solution is that which is closest to the value inferred by the algorithm. The technique is trained on Monte Carlo, and its effectiveness is evaluated using generator-level information in which the true Λ_b^0 momentum is known.

The ability to select the best Λ_b^0 momentum solution will be assessed by comparing the q^2 distributions resulting from either technique (linear-regression choice, or lowest-boost solution), and comparing with the q^2_{True} distribution using generator level simulated events. An example of the resolution for each technique is shown in figure 35, however further refinement of the linear regression method may show an improved result. Regardless, one technique will be used for the determination of Λ_b^0 momentum, and the other used to estimate the systematic uncertainty related to the method used.

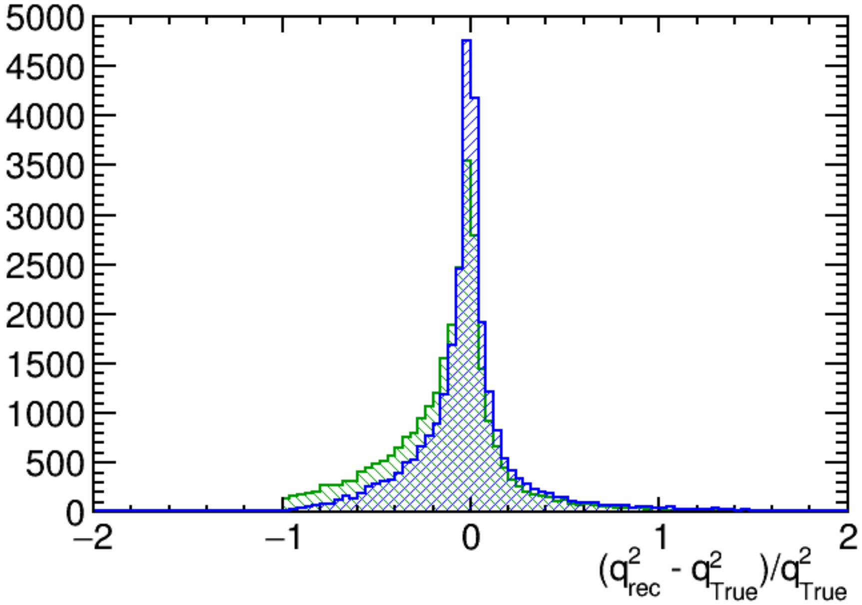

Figure 35: Resolution of reconstructed q^2 verses true q^2 for the two techniques of selecting the Λ_b^0 momentum solution: the low-boost solution (blue), and the q^2 derived from the linear regression method described in the text.

4.3.4 Templates for the Corrected Mass Fit

The method for extracting the raw yield of $\Lambda_b^0 \to \Lambda_c^+ \mu^- \overline{\nu}_\mu$ events involves fitting to the corrected mass distribution for the $\Lambda_b^0 \to \Lambda_c^+ \mu^- \overline{\nu}_\mu X$ data sample. The shape of the signal and various background components are modeled by templates from simulated events. The modeling of the double-charm background is based on simulated events of $\Lambda_b^0 \to \Lambda_c^+ D_s^-$ where the D_s^- decays either leptonically or semileptonically. We are studying variations of the background PDFs based on the presence of additional $b \to c\bar{c}$ modes and tauonic semileptonic decays. Additional studies incorporating some of these components is still ongoing.

4.4 Refinement of the V_{cb} Measurement

The lattice predictions are more precise at the zero-recoil region, thus a study of the spectrum $d\Gamma/dq^2$ is going to give a more precise estimate of $|V_{cb}|$, as well as aiding the evaluation of the systematic effects due to form factor uncertainty.

The theoretical prediction for $\Gamma_{Th.}(\Lambda_b^0 \to \Lambda_c^+ \mu^- \overline{\nu}_\mu)$ has also been presented in Ref. [9] in seven q^2 bins. To obtain a more accurate measurement of $|V_{cb}|$, the analysis will be done in q^2 bins to obtain a measured spectra $d\Gamma_{Meas.}(\Lambda_b^0 \to \Lambda_c^+ \mu^- \overline{\nu}_\mu)/dq^2$.

The differential distribution dN_{corr}/dq^2 must be obtained using the same method as described for the total distribution. Fits to the Λ_b^0 corrected mass will be done in 10 q^2 bins to obtain dN_{Raw}/dq^2.

4.4.1 Unfolding the dN_{Raw}/dq^2 Spectrum

In order to compare the measured $d\Gamma/dq^2$ with theoretical predictions, it is necessary to take into account the smearing of the parent spectrum due to the finite detector resolution: this mapping of $d\Gamma/dq^2{}_{\mathrm{meas}}$ into $d\Gamma/dq^2$ is generally known as "unfolding."

Since the predicted $d\Gamma_{Th.}(\Lambda_b^0 \to \Lambda_c^+ \mu^- \overline{\nu}_\mu)/dq^2$ is reported in seven q^2 bins. It is known that in order to make the unfolding process more robust, more bins in inferred q^2 than in "true" q^2 are necessary. Thus we determine raw yields in ten bins of reconstructed q^2 bins, and we unfold them in seven true q^2 bins. Generator-level simulation is used to find the unfolding matrix, mapping the population in true q^2 distribution to spectral distribution in reconstructed q^2.

Preliminary studies using the RooUnfold package [31] have been done. The inversion of the response matrix in the unfolding stage require some care, as small off diagonal matrix elements can lead to unstable results. Thus a regularization procedure is needed: our primary choice is the Single Value Decomposition (SVD) approach [32], which relies on the *effective rank* parameter k, which gives the number of significant terms in the decomposition. The value of k will also be studied, with different choices used to assess systematic uncertainties. An alternative method, a Bayesian approach derived by De Agostini, will be used to validate the robustness of our approach.

The unfolded $dN_{unfold.}/dq^2$ distribution will then be corrected for detector efficiencies and charm branching fractions in an identical manner as described previously: the efficiency will be computed for each of the seven q^2_{True} bins, and applied to the data accordingly, to obtain $dN_{corr.}/dq^2$. This spectrum will be normalized by $N_{corr}(\Lambda_b^0\ X_c \mu^- \overline{\nu}_\mu)$ as before, and the measured $d\Gamma(\Lambda_b^0 \to \Lambda_c^+ \mu^- \overline{\nu}_\mu)/dq^2$ will be obtained.

Finally, a joint fit to the measured and predicted spectra $d\Gamma(\Lambda_b^0 \to \Lambda_c^+ \mu^- \overline{\nu}_\mu)/dq^2$ will be performed to extract a more accurate determination of $|V_{cb}|$. The shape of the differential distribution is given by equation 85 of [9], which includes $|V_{cb}|^2$ as a normalization parameter. Comparison between theory and experiment with different q^2 cuts can further elucidate the stability of our result, and the robustness of the theoretical uncertainty. Lastly we can examine the sensitivity to the form factor parameterization (normalization and shape), with fits that allow theoretical parameters to float or are constrained by HQET [33]. These different fits will allow to pin down the sensitivity of $|V_{cb}|$ to theoretical inputs.

5 Conclusions

A method for determining $|V_{cb}|$ from the exclusive decay $\Lambda_b^0 \to \Lambda_c^+ \mu^- \overline{\nu}_\mu$ has been presented. Raw yields for the signal decay are determined by fitting to the Λ_b^0 corrected mass, and are corrected for detector and reconstruction efficiencies and the charm branching fraction $\mathcal{B}(\Lambda_c^+ \to pK^-\pi^+)$ to obtain $N_{corr}(\Lambda_b^0 \to \Lambda_c^+ \mu^- \overline{\nu}_\mu)$. This is normalized to the corrected yield $N_{corr}(\Lambda_b^0 \to X_c \mu^- \overline{\nu}_\mu)$, which includes contributions from $\Lambda_b^0 \to \Lambda_c^{+*} \mu^- \overline{\nu}_\mu$ and $\Lambda_b^0 \to D^0 p \mu^- \overline{\nu}_\mu$ decays. The semileptonic width $\Gamma_{Meas.}(\Lambda_b^0 \to \Lambda_c^+ \mu^- \overline{\nu}_\mu)$ is determined from the corrected & normalized yield. Lattice QCD calculations predict $\Gamma_{Meas.}(\Lambda_b^0 \to \Lambda_c^+ \mu^- \overline{\nu}_\mu)/|V_{cb}|^2$. Comparing the measured width to the lattice QCD prediction provides the measurement

$$|V_{cb}| = (44.1 \pm 1.01) \times 10^{-3}$$

The method used to extract $N_{corr}(\Lambda_b^0 \to \Lambda_c^+ \mu^- \overline{\nu}_\mu)$ and $N_{corr}(\Lambda_b^0 \to X_c \mu^- \overline{\nu}_\mu)$ also allows for a determination of the branching fraction $\mathcal{B}(\Lambda_b^0 \to \Lambda_c^+ \mu^- \overline{\nu}_\mu)$ by using well measured properties of lighter B-meson decays. The measured branching fraction is

$$\mathcal{B}(\Lambda_b^0 \to \Lambda_c^+ \mu^- \overline{\nu}_\mu) = (6.30 \pm 0.39)\%$$

Uncertainties reported are statistical. Further study of the systematic uncertainties on each measurement is required and is currently ongoing. Furthermore, a more accurate technique of determining $|V_{cb}|$ is defined and is being refined.

References

[1] CKMfitter group, J. Charles *et al.*, *Current status of the Standard Model CKM fit and constraints on $\Delta F = 2$ new physics*, Phys. Rev. **D91** (2015) 073007, `arXiv:1501.05013`, updated results and plots available at `http://ckmfitter.in2p3.fr/`.

[2] Heavy Flavor Averaging Group, Y. Amhis *et al.*, *Averages of b-hadron, c-hadron, and τ-lepton properties as of summer 2016*, Eur. Phys. J. **C77** (2017) 895, `arXiv:1612.07233`, updated results and plots available at `http://www.slac.stanford.edu/xorg/hflav/`.

[3] UTfit collaboration, M. Bona *et al.*, *The unitarity triangle fit in the standard model and hadronic parameters from lattice QCD: A reappraisal after the measurements of Δm_s and $BR(B \to \tau\nu_\tau)$*, JHEP **10** (2006) 081, `arXiv:hep-ph/0606167`, updated results and plots available at `http://www.utfit.org/`.

[4] Particle Data Group, C. Patrignani *et al.*, *Review of particle physics*, Chin. Phys. **C40** (2016) 100001, and 2017 update.

[5] I. I. Bigi, T. Mannel, and N. Uraltsev, *Semileptonic width ratios among beauty hadrons*, JHEP **09** (2011) 012, `arXiv:1105.4574`.

[6] A. J. Buras and E. Venturini, *Searching for New Physics in Rare K and B Decays without $|V_{cb}|$ and $|V_{ub}|$ Uncertainties*, `arXiv:2109.11032`.

[7] ALPHA collaboration, J. Heitger and R. Sommer, *Nonperturbative heavy quark effective theory*, JHEP **02** (2004) 022, `arXiv:hep-lat/0310035`.

[8] N. Isgur and M. B. Wise, *Heavy baryon weak form-factors*, Nucl. Phys. B **348** (1991) 276.

[9] W. Detmold, C. Lehner, and S. Meinel, *$\Lambda_b \to p\ell^-\bar{\nu}_\ell$ and $\Lambda_b \to \Lambda_c\ell^-\bar{\nu}_\ell$ form factors from lattice QCD with relativistic heavy quarks*, Phys. Rev. D **92** (2015) 034503, `arXiv:1503.01421`.

[10] LHCb collaboration, R. Aaij *et al.*, *Measurement of the shape of the $\Lambda_b^0 \to \Lambda_c^+\mu^-\overline{\nu}_\mu$ differential decay rate*, Phys. Rev. D **96** (2017) 112005, `arXiv:1709.01920`.

[11] LHCb collaboration, R. Aaij *et al.*, *Framework TDR for the LHCb Upgrade: Technical Design Report*, CERN **CERN-LHCC-2012-007** (2012).

[12] LHCb collaboration, R. Aaij *et al.*, *LHCb VELO (VErtex LOcator): Technical Design Report*, CERN **Technical design report. LHCb** (2001) 97.

[13] LHCb collaboration, R. Aaij *et al.*, *LHCb Tracker Upgrade Technical Design Report*, CERN **Technical design report. LHCb** (2014) 15.

[14] LHCb collaboration, R. Aaij *et al.*, *LHCb PID Upgrade Technical Design Report*, CERN **Technical design report LHCb** (2013) 14.

[15] LHCb collaboration, R. Aaij *et al.*, *LHCb magnet: Technical Design Report*, CERN **Technical design report. LHCb** (2000) 1.

[16] LHCb collaboration, R. Aaij *et al.*, *LHCb RICH: Technical Design Report*, CERN **Technical design report. LHCb** (2000) 92.

[17] LHCb collaboration, R. Aaij *et al.*, *LHCb calorimeters: Technical Design Report*, CERN **Technical design report. LHCb** (2000) 116.

[18] LHCb collaboration, O. Deschamps *et al.*, *Photon and Neutral Pion Reconstruction*, CERN **CERN-LHCb-2003-091** (2003).

[19] LHCb collaboration, R. Aaij *et al.*, *Design and performance of the LHCb trigger and full real-time reconstruction in Run 2 of the LHC*, JINST **14** (2019) P04013, `arXiv:1812.10790`.

[20] LHCb Collaboration, R. Aaij *et al.*, *Measurement of b hadron production fractions in 7 TeV pp collisions*, Phys. Rev. D **85** (2011) 032008. 28 p, `arXiv:1111.2357`, Comments: 28 pages, 12 figures.

[21] LHCb collaboration, M. Williams *et al.*, *The HLT2 Topological Lines*, CERN **CERN-LHCb-PUB-2011-002** (2011).

[22] LHCb collaboration, A. Jaeger *et al.*, *Measurement of the Track Finding Efficiency*, CERN **CERN-LHCb-PUB-2011-025** (2011).

[23] LHCb collaboration, T. S *et al.*, *Data Driven Trigger Efficiency Determinatino at LHCb*, CERN **CERN-LHCb-PUB-2014-039** (2014).

[24] LHCb collaboration, L. Anderlini *et al.*, *The PIDCalib Package*, CERN **CERN-LHCb-PUB-2016-021** (2016).

[25] M. Pivk and F. R. Le Diberder, *sPlot: A statistical tool to unfold data distributions*, Nucl. Instrum. Meth. **A555** (2005) 356, `arXiv:physics/0402083`.

[26] LHCb Collaboration, R. Aaij *et al.*, *Measurement of b hadron fractions in 13 TeV pp collisions*, Phys. Rev. D **100** (2019) , `arXiv:1902.06794`.

[27] LHCb Collaboration, R. Aaij *et al.*, *Study of the* D^0p *amplitude in* $\Lambda_b^0 \to D^0 p\pi^-$*decays*, Journal of High Energy Physics **30** (2017) , `arXiv:1701.07873`.

[28] Belle Collaboration, A. Zupanc *et al.*, *Measurement of the Branching Fraction* $B(\Lambda_c \to pK^-\pi^+)$, Phys. Rev. Letters **113** (2014) , `arXiv:1312.7826`.

[29] CLEO Collaboration, G. Bonvicini *et al.*, *Updated measurements of absolute* D^+ *and* D^0 *hadronic branching fractions and* $\sigma(e^+e^- \to D\overline{D})$ *at* $E_{cm} = 3774MeV$, Phys. Rev. D **89** (2014) .

[30] F. Pedregosa and others, *Scikit-learn: Machine Learning in Python*, Journal of Machine Learning Research **12** (2011) 2825.

[31] T. Adye, *Unfolding algorithms and tests using RooUnfold*, in *Proceedings, PHYSTAT 2011 Workshop on Statistical Issues Related to Discovery Claims in Search Experiments and Unfolding, CERN,Geneva, Switzerland 17-20 January 2011*, (Geneva), 313–318, CERN, CERN, 2011, `arXiv:1105.1160`.

[32] A. Hoecker and V. Kartvelishvili, *SVD Approach to Data Unfolding*, Nuclear Instruments and Methods in Physics Research Section A: Accelerators, Spectrometers, Detectors and Associated Equipment **372** (1996) 469, `arXiv:9509307`.

[33] F. U. Bernlochner, Z. Ligeti, D. J. Robinson, and W. L. Sutcliffe, *New predictions for* $\Lambda_b \to \Lambda_c$ *semileptonic decays and tests of heavy quark symmetry*, Phys. Rev. Lett. **121** (2018) 202001, `arXiv:1808.09464`.

Dr. Scott Edward Ely

Personal Data

Name	Dr. Scott Ely
Gender	Male
Address	10C Brackenbury Gardens, London, United Kingdom, W6 0BP
Phone	+1 510 648 5856
email	scottely@outlook.com

Work Experience

07/2022–Present	Post Doctoral Research Assistant at Imperial College of Science, Technology, and Medicine
11/2021–07/2022	Post Doctoral Research Assistant at Syracuse University
08/2013–11/2021	Graduate Research Assistant at Syracuse University
06/2012–06/2013	Research Assistant at The University of California: Santa-Cruz

Education

07/2022 Ph.D in Physics

Syracuse University

Thesis Title: Measurement of $|V_{cb}|$ using the Semileptonic Decay $\Lambda_b \rightarrow \Lambda_c \mu \overline{\nu}_\mu$

06/2012 B.S. in Applied Physics

University of California: Santa-Cruz

Thesis Title: Progress in Scribe-Cleave-Passivate Method to Create Slim Edges for N-Type Silicon Strip Detectors

Research Experience and Interests

LHCb Collaboration at the Large Hadron Collider
Upstream Tracker (UT Upgrade) 2013–Present

- UT Commissioning Coordinator: Responsible for managing the assembly and installation of the UT detector at the LHCb experiment site.
- Preparation, integration, and commissioning of populated staves and infrastructure onto the UT detector.
- Collaboration with CERN IRRAD to arrange irradiation of components to simulate damage over time.
- Planning and execution of test beam experiments to study UT components in a particle beam.
- Silicon sensor performance techniques, including IV, CV, and long-term stability tests.
- Studies of semileptonic B decays, especially the decays $\Lambda_b \to \Lambda_c^{(*)}\mu\overline{\nu}_\mu$.

Santa Cruz Institute for Particle Physics (SCIPP)
RD50 Collaboration 2012–2013

- Preliminary tests of Low-Gain Avalanche Diodes (LGAD), to study prospects of constructing fast-timing silicon sensors.
- Silicon sensor characterization to study techniques to create slim-edge devices.

Selected Publications

- Measurement of b-Hadron Fractions in 13 TeV pp Collisions R. Aaij et al. (**incl. S. Ely**)
  Phys. Rev. D in February 2019
  https://arxiv.org/abs/1902.06794
- Measurement of the Shape of the $\Lambda_b \to \Lambda_c\mu\overline{\nu}_\mu$ Differential Decay Rate
  R. Aaij et al. (**incl. S. Ely**), Phys. Rev. D 96 (2017), 112005
  https://journals.aps.org/prd/cited-by/10.1103/PhysRevD.96.112005
- Measurement of the b-quark Production Cross Section in 7 and 13 TeV pp Collisions
  R. Aaij et al. (**incl. S. Ely**), Phys. Rev D 118 (2017), 052002, Erratum: Phys. Rev. D 119 (2017), 169901
  Original: https://journals.aps.org/prl/abstract/10.1103/PhysRevLett.118.052002
  Erratum: https://journals.aps.org/prl/abstract/10.1103/PhysRevLett.119.169901
- Sensors for Ultra-Fast Silicon Detectors
  H. F. -W. Sadrozinski et al (**incl S. Ely**)
  Nuclear Inst. And Methods in Physics Research, A, Vol. 765, p. 7-11 (2014)

Selected Conference Presentations

- Construction and Commissioning of the LHCb Upstream Tracker. April APS Meeting 2021, Session L20: LHC Detector Upgrades 17-20 April 2021
- Silicon Test Beam Results for the LHCb-UT Detector. 2017 US LHC Users Association Meeting. Young Physicists' Lightning Round. 3 November 2017
- Pulse Shapes of Alpha Particles in CNM Diodes With and Without Gain 22nd RD50 Workshop, Albuquerque, USA. 3-5 June 2013

Awards

- 2021 LHCb Early Career Scientist Award
  - For extraordinary leadership of the UT project.
- 2017 US LHC USers Association Young Physicist Lightning Round Winner
  - Presentation Title: Silicon Test Beam Results for the LHCb-UT Detector.